Mechanism of nucleation and incipient growth of Re clusters in irradiated W-Re alloys from kinetic Monte Carlo simulations

Chen-Hsi Huang,[1] Leili Gharaee,[2] Yue Zhao,[1] Paul Erhart,[2] and Jaime Marian[1,3]
[1]*Department of Materials Science and Engineering, University of California, Los Angeles, California 90095, USA*
[2]*Department of Physics, Chalmers University of Technology, S-412 96 Gothenburg, Sweden*
[3]*Department of Mechanical and Aerospace Engineering, University of California, Los Angeles, California 90095, USA*
(Received 6 February 2017; revised manuscript received 24 July 2017; published 18 September 2017)

High-temperature, high-dose, neutron irradiation of W results in the formation of Re-rich clusters at concentrations one order of magnitude lower than the thermodynamic solubility limit. These clusters may eventually transform into brittle W-Re intermetallic phases, which can lead to high levels of hardening and thermal conductivity losses. Standard theories of radiation-enhanced diffusion and precipitation cannot explain the formation of these precipitates and so understanding the mechanism by which nonequilibrium clusters form under irradiation is crucial to predict material degradation and devise mitigation strategies. Here we carry out a thermodynamic study of W-Re alloys and conduct kinetic Monte Carlo simulations of Re cluster formation in irradiated W-2Re alloys. We use a generalized Hamiltonian for crystals containing point defects parametrized entirely with electronic structure calculations. Our model incorporates recently gained mechanistic information of mixed-interstitial solute transport, which is seen to control cluster nucleation and growth by forming quasispherical nuclei after an average incubation time of 13.5($\pm$8.5) s at 1800 K. These nuclei are seen to grow by attracting more mixed interstitials bringing solute atoms, which in turn attracts vacancies leading to recombination and solute agglomeration. Owing to the arrival of both Re and W atoms from the mixed dumbbells, the clusters are not fully dense in Re, which amounts to no more than 50% of the atomic concentration of the cluster near the center. Our simulations are in qualitative agreement with recent atom probe examinations of ion-irradiated W-2Re systems at 773 K.

DOI: 10.1103/PhysRevB.96.094108

I. INTRODUCTION

Tungsten is being considered as a candidate structural material in magnetic fusion energy devices due to its high strength and excellent high-temperature properties [1–4]. Upon fast neutron irradiation in the 600–1000 °C temperature range, W transmutes into Re by the way of β-decay reactions at a rate that depends on the neutron spectrum and the position in the reactor. For the DEMO (DEMOnstration fusion power plant) reactor concept, calculations show that the transmutation rate is 2000 and 7000 atomic parts per million (appm) per displacement per atom (dpa) in the divertor and the equatorial plane of the first wall, respectively (in each case, damage accumulates at rates of 3.4 and 4.4 dpa/year) [5,6]. The irradiated microstructure initially evolves by accumulating a high density of prismatic dislocation loops and vacancy clusters, approximately up to 0.15 dpa [7–10]. Subsequently, a void lattice emerges and fully develops at fluences of around 1 dpa. After a critical dose that ranges between 5 dpa for fast (>1 MeV) neutron irradiation [9] and 2.2 dpa in modified target rabbits in the HFIR [10,11], W and W-Re alloys develop a high density of nanometric precipitates with acicular shape at Re concentrations well below the solubility limit [9,10]. The structure of these precipitates is consistent with σ (W_7Re_6) and χ (WRe_3) intermetallic phases, which under equilibrium conditions only occur at temperatures and Re concentrations substantially higher than those found in neutron irradiation studies [12]. A principal signature of the formation of these intermetallic structures in body-centered cubic (bcc) W is the sharp increase in hardness and embrittlement [8–10]. Qualitatively similar observations have been recently made in W-2Re and W-1Re-1Os alloys subjected to heavy-ion irradiation [13,14], clearly establishing a link between primary damage production and Re precipitation. Figure 1 shows the phase diagram of W-Re from modern analysis [15–17], clearly showing the solubility limit of Re in W, as well as the region of existence of the σ and χ phases.

Precipitation of nonequilibrium phases in irradiated materials is commonplace. The standard theory of irradiation damage includes radiation-enhanced diffusion (RED) and radiation-induced precipitation (RIP) as mechanisms that can drive the system out of equilibrium due to the onset of point defect cluster fluxes towards defect sinks [18–20]. Within this picture, Re precipitation in W or W-Re alloys under irradiation would then, in principle, be unsurprising were it not for the fact that Re clustering is seen to occur at concentrations still below the solubility limit even after RED has taken place. Recent work using energy models based on the cluster expansion formalism for the W-Re system, and fitted to density functional theory (DFT) calculations, has revealed a direct relationship between excess vacancy concentrations and the formation of Re-solute-rich clusters [21]. These calculations are substantiated by recent neutron irradiation experiments of pure W at 900 °C up to 1.6 dpa in the HFR in Petten [22]. Postirradiation examination of the irradiated specimens reveals the formation of a fine distribution of voids with average 5 nm size surrounded by Re-rich clouds. However, the relative concentration of Re around the voids is still on the order of 12%–18% (from a nominal overall concentration of 1.4% from transmutation), well below the precipitation limit of Re in W at 900 °C. However, in the ion beam irradiation experiments of W-2Re alloys by Xu *et al.* at 300 and 500 °C, Re-rich clusters with bcc structure are seen to form with concentrations between 12% and 30% Re with no indication of vacancies

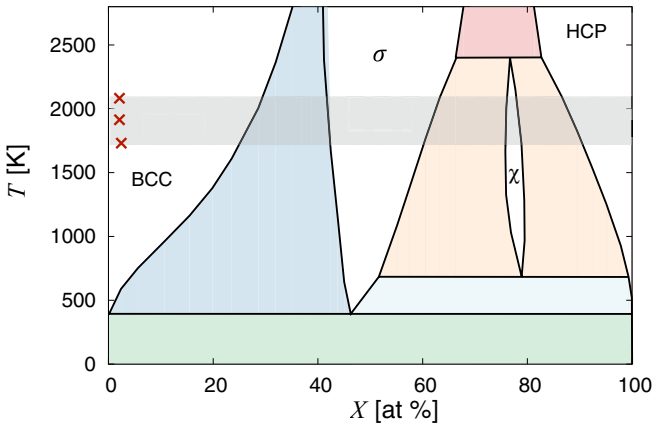

FIG. 1. Re-W phase diagram. The shaded region corresponds to the temperature range explored in the kMC simulations, while the crosses mark the 2% Re concentration point (adapted from Ref. [16]).

forming part of the clusters [13,14]. Another piece of evidence against a strong association between vacancies and Re atoms comes from irradiation tests of W-Re alloys performed at EBR-II in the 1970s and 1980s [23–27]. In these studies, the presence of Re was seen to suppress swelling, which would seem to suggest a decoupling between vacancy clusters and Re atoms. Clearly, equilibrium thermodynamics involving vacancies alone may not suffice to explain the precipitation tendencies in irradiated W-Re alloys.

All this is suggestive of alternative solute transport mechanisms that may be unique to W-Re systems. Indeed, several recent studies using electronic structure calculations have independently reported a peculiar association between self-interstitial atoms (SIAs) and Re solutes that results in very high solute transport efficacy [28–30]. This mechanism consists of a series of mixed dumbbell rotations and translations such that the mixed nature of the dumbbell is preserved and solutes can be transported over long distances without the need for vacancy exchanges. Furthermore, this mechanism effectively transforms one-dimensional SIA diffusion into a 3D mixed-dumbbell transport process at activation energies considerably lower than that of vacancy diffusion. The objective of this paper is to study the kinetics of Re-cluster nucleation and incipient growth in irradiated W accounting for both vacancy and mixed-interstitial solute transport. To this effect, we develop a lattice kinetic Monte Carlo (kMC) model of alloy evolution parametrized solely using first-principles calculations. We start in Sec. II by describing the essential elements of our kinetic model as well as the parametrization effort based on DFT calculations. In Sec. III we provide our main results, including semi-grand-canonical Monte Carlo calculations of ternary W-Re-vacancy and W-Re-SIA systems, and kMC simulations and analysis of the Re-precipitate nucleation and growth. We finish with a discussion of the results and the conclusions in Sec. IV.

II. THEORY AND METHODS

A. Energy model

The energy model employed in this work is a cluster expansion Hamiltonian based on pair interactions truncated at the second-nearest-neighbor (2nn) shell:

$$\mathscr{H} = \sum_i \sum_{\alpha,\beta} n^{(i)}_{\alpha\text{-}\beta} \varepsilon^{(i)}_{\alpha\text{-}\beta}, \tag{1}$$

where (i) specifies the type of nearest-neighbor interaction (first or second), α and β refer to a pair of lattice sites, separated by a distance specified by the index i, $n_{\alpha\text{-}\beta}$ denotes the number of occurrences (bonds) of each α-β pair, and $\varepsilon_{\alpha\text{-}\beta}$ is the bond energy. In a previous work, we have shown how this Hamiltonian can be reduced to a generalized Ising Hamiltonian involving solvent and solute atoms (A and B), vacancies (V), and pure and mixed interstitials (AA, BB, and AB) [31]. The Hamiltonian is then expressed as a sum of polynomial terms of various degrees involving spin variables σ_α and σ_β in the manner of the Ising model:

$$\mathscr{H} = \sum_{n,m} \sum_{\alpha,\beta} C_{nm} \sigma^n_\alpha \sigma^m_\beta, \tag{2}$$

where n and m are exponents reflecting the order of each term, and C_{nm} are the set of coupling constants. One of the advantages of using this notation is that the values assigned to the spin variables conserve the number of atoms N of the system. We refer the reader to Ref. [31] for more details about this notation. In this paper we focus on the parametrization exercise for irradiated W-Re alloys.[1]

B. Semi-grand-canonical Monte Carlo for AB systems

The thermodynamic phase diagram of the W-Re system can be studied using semi-grand-canonical Monte Carlo (SGMC) calculations as a function of temperature and solute concentration [32–37]. In SGMC, we seek to minimize the thermodynamic potential of the semi-grand-canonical ensemble, characterized by a constant temperature T, a constant number of particles N, and a constant chemical potential μ.[2] In each SGMC step, a transition involving an atom selected at random is executed and the new state is accepted with a probability

$$p_{ij} = \exp\left(-\frac{\Delta\mathscr{H}_{ij} - N_\mathrm{B}\Delta\mu}{k_B T}\right), \tag{3}$$

where $\Delta\mathscr{H}_{ij}$ is the energy difference between the initial and final states, i and j, $N_\mathrm{B} = NX$ is the number of solute atoms (X: solute concentration), $\Delta\mu$ is the change in chemical potential per atom after the transition, and k_B is Boltzmann's constant. In this work, each transition is defined by changing the chemical nature of one atom chosen at random (A $\rightarrow$ B or B $\rightarrow$ A). In terms of the change in spin variable [in the notation of the generalized Ising Hamiltonian; cf. Eq. (2)], this always results in a change of $\delta\sigma = \pm 2$, such that Eq. (3) can be simplified to

$$p_{ij} = \exp\left(-\frac{\Delta\mathscr{H}_{ij} \pm 2\Delta\mu}{k_B T}\right). \tag{4}$$

[1]We use the notation A: W atoms; B: Re atoms; V: vacancies, AA: W-W dumbbell (or self-interstitial atom); BB: Re-Re dumbbell; AB: mixed W-Re dumbbell.

[2]For a brief discussion on the differences between the semi-grand-canonical and the grand-canonical ensembles, see Ref. [38].

In the calculations, the chemical potential difference $\Delta\mu$ and the temperature T are input variables, while the solute composition X and the equilibrium configurations are obtained when convergence is reached.

C. Metropolis Monte Carlo calculations of ABV system configurations

During irradiation, the introduction of large amounts of defects has the potential to impact the thermodynamics of the system. It is therefore of interest to calculate phase diagrams with fixed defect concentrations using equilibrium (Metropolis) Monte Carlo. Defect concentrations are not thermodynamically equilibrated under irradiation—the number of vacancies or interstitials is not controlled by the chemical potential—and so the AB system must be considered in conjunction with a fixed defect concentration. Take the case of vacancies, for example: to properly obtain converged nonequilibrium configurations of ABV systems, we employ a *flip* and *swap* approach: (i) initially a system consisting of A atoms and a random distribution of vacancies is considered; (ii) a lattice point is selected at random; (iii) if that lattice point corresponds to an atom, a SGMC step is carried out, resulting in a change in the relative concentrations of A and B; if it, on the contrary, corresponds to a vacant site, then a canonical Monte Carlo step is carried out, leaving X unchanged, and the vacancy exchanges its position with a randomly selected atom. This trial swap is then accepted according to the Boltzmann distribution:

$$p_{ij} = \exp\left(-\frac{\Delta\mathscr{H}_{ij}}{k_B T}\right). \tag{5}$$

In this fashion, equilibrated AB alloys containing a fixed vacancy concentration are obtained, from which one can determine the changes relative to the thermodynamic equilibrium configurations. Although interstitials are much higher in energy than vacancies (so that only very small concentrations need be explored), the procedure for the ABI system is identical to that of the ABV system.

D. Kinetic Monte Carlo simulations of ABVI systems

The kinetic evolution of W-Re alloys under irradiation is studied using standard lattice kMC. The system is evolved by events involving atomic jumps and time is advanced according to the residence-time algorithm [39]. Jump rates are calculated as

$$r_{ij} = \nu \exp\left(-\frac{\Delta E_{ij}}{k_B T}\right), \tag{6}$$

where ν is an attempt frequency and ΔE_{ij} is the activation energy to jump from state i to state j.

1. Vacancy migration model

Several models have been proposed to describe the activation energy based on different interpretations of the atomic migration process (see, e.g., [31,40] for recent reviews). In this work, the activation energy of vacancy jump is calculated by the saddle-point energy model (or cut-bond model) [41–44], according to which ΔE_{ij} is given by the energy difference of the configuration when the jumping atom is at the saddle point and the initial configuration

$$\Delta E_{ij} = \sum_p \varepsilon^{sp}_{\alpha\text{-}p} - \sum_q \varepsilon^{(i)}_{\alpha\text{-}q} - \sum_{r\neq\alpha} \varepsilon^{(i)}_{\mathrm{V}\text{-}r} + \sum \Delta E^{\mathrm{nonbroken}}_{ij}, \tag{7}$$

where α is the jumping atom, V is the vacancy, and ε^{sp} are the bond energies between the atom at the saddle point and the neighboring atoms. The first term on the right-hand side of Eq. (7) reflects the energy of the jumping atom at the saddle point. In this work, we consider interactions up to 2nn distances for this term.[3] The second and third terms on the right-hand side of the equation are the energies of the jumping atom and the vacancy at the initial state i. Finally, the fourth term gives the energy difference between state i and j for the nonbroken bonds due to local solute concentration changes. The dependence of bond coefficients on local solute concentration will be discussed in Sec. II E.

2. Interstitial defect migration model

Here we consider self-interstitial atoms of the AA type, and mixed-interstitials AB. Due to their rarity, BB interstitials are omitted in our calculations. In bcc metals, AA SIAs are known to migrate athermally in one dimension along ⟨111⟩ directions with migration energy E_m, with sporadic rotations to other ⟨111⟩ orientations characterized by an activation energy E_r. These processes, however, are treated separately in the kMC simulations. In contrast to vacancy migration, activation energies of interstitial jumps are calculated using the direct final-initial system energy model [45–48]:

$$\Delta E_{ij} = \begin{cases} E_m + \Delta\mathscr{H}_{ij}, & \text{if } \Delta\mathscr{H}_{ij} > 0, \\ E_m, & \text{if } \Delta\mathscr{H}_{ij} < 0, \end{cases} \tag{8}$$

where $\Delta\mathscr{H}_{ij}$ is the same as in Eq. (5). In addition, we include a bias due to the well-known phenomenon of *correlation*, by which a forward jump is slightly more likely to occur than a backward jump. This is reflected in a correlation factor f computed as the ratio of forward to backward jumps [49], which in our simulations is temperature dependent.

For their part, as pointed out in Sec. I, recent DFT studies have revealed a new migration mechanism for mixed dumbbells in W alloys. This mechanism involves a nondissociative sequence of rotations and translations such that the solute atom is always part of the mixed dumbbell (in contrast with the *interstitialcy* or "knock-on" mechanism commonly associated with SIAs) [28–30,50]. This effectively makes AB interstitials move in three dimensions with 2nn jumps along ⟨100⟩ directions. Calculations for the W-Re system have shown that the migration energy in this case is very low, on the order of one tenth of an eV. As we shall see, this plays a important role in governing the kinetic evolution of irradiated W-Re alloys.

[3] In the saddle-point configuration for vacancy migration, there are six 1nn bonds and six 2nn bonds, compared with eight and six for a lattice point configuration.

3. *Spontaneous events: Recombination and absorption*

Any recombination event occurs spontaneously (no sampling involved) when the distance between an interstitial defect and a vacancy is within the third-nearest-neighbor distance. Another reaction considered to be instantaneous is the transition of a SIA into an AB dumbbell when it encounters a solute atom: $\mathrm{AA} + \mathrm{B} \rightarrow \mathrm{AB} + \mathrm{A}$. This is because the binding energy between a SIA and a Re solute atom has been calculated to be -0.8 eV (negative binding energies represent attraction). The distance for this transformation is set to be equal to the 1nn separation.

Defect absorption represents another type of spontaneous event. Absorption can occur at sinks, such as a plane located in a stationary position within the simulation box [51], or a free surface [31]. Sinks can potentially act also as defect emitters, as in the case of grain boundaries, dislocations, and free surfaces in real microstructures. Details about the implementation of these processes can be found in Ref. [31].

4. *Frenkel pair generation*

In this work, defects are generated as Frenkel pairs at a prescribed rate set by the damage rate. To insert a defect pair, two atomic sites are chosen at random; one is replaced by a vacancy, and the other with an interstitial formed by an A atom and the lattice atom.

E. Parameters

There are five distinct atomic species used in this work: W atoms (A), Re atoms (B), vacancies (V), SIAs (AA), and mixed-interstitials (AB). As mentioned above, our energy model consists of pairwise interactions up to the 2nn shell. After discounting interstitial-vacancy bonds, this amounts to 26 different types of bonds (13 for each nearest-neighbor shell), all of which must be obtained using first-principles calculations. Moreover, as discussed by Martinez *et al.* [43] and Senninger *et al.* [44], several of these bond energies are sensitive to the local solute concentration and must be computed on the fly in each Monte Carlo step. Following Warczok *et al.* [52], we reduce the number of unknowns from 26 to 13 by partitioning bond energies according the following relation:

$$\varepsilon^{(2)} = \varepsilon^{(1)} \left(\frac{r_{2\mathrm{nn}}}{r_{1\mathrm{nn}}} \right)^{-6}, \tag{9}$$

which is used unless both bond energies can be explicitly calculated. For the bcc lattice, this results in $\varepsilon^{(2)}_{\alpha\text{-}\beta}/\varepsilon^{(1)}_{\alpha\text{-}\beta} = 0.421875$ for regular bond coefficients, and $\varepsilon^{sp(2)}_{\alpha\text{-}\beta}/\varepsilon^{sp(1)}_{\alpha\text{-}\beta} = 0.194052$ for saddle-point bond coefficients.

The local solute concentration is always computed up to the 2nn shell. Next we describe the parametrization procedure for each set of bond energies.

1. *W-Re parameters*

The W-Re bond coefficients are $\varepsilon_{\mathrm{A\text{-}A}}$, $\varepsilon_{\mathrm{B\text{-}B}}$, and $\varepsilon_{\mathrm{A\text{-}B}}$. They determine the thermodynamic equilibrium phase diagram of the alloy. $\varepsilon_{\mathrm{A\text{-}A}}$ and $\varepsilon_{\mathrm{B\text{-}B}}$ are obtained from the cohesive energies:

$$E^{\mathrm{A}}_{\mathrm{coh}} = -\frac{z_1}{2}\varepsilon^{(1)}_{\mathrm{A\text{-}A}} - \frac{z_2}{2}\varepsilon^{(2)}_{\mathrm{A\text{-}A}},$$
$$E^{\mathrm{B}}_{\mathrm{coh}} = -\frac{z_1}{2}\varepsilon^{(1)}_{\mathrm{B\text{-}B}} - \frac{z_2}{2}\varepsilon^{(2)}_{\mathrm{B\text{-}B}}, \tag{10}$$

where z_1 and z_2 are coordination numbers for the 1nn and 2nn shells, respectively. The cohesive energies calculated using DFT are given in Table I.[4]

The coefficient for the A-B bond is obtained from the enthalpy of mixing of W-Re, ΔH^{mix}, which can be written within the Bragg-Williams approximation [56–58] as

$$\Delta H^{\mathrm{mix}} = \frac{z_1}{2}\left[(1-X)\varepsilon^{(1)}_{\mathrm{A\text{-}A}} + X\varepsilon^{(1)}_{\mathrm{B\text{-}B}} + 2x(1-x)\Omega^{(1)}_s\right] + \frac{z_2}{2}\left[(1-X)\varepsilon^{(2)}_{\mathrm{A\text{-}A}} + X\varepsilon^{(2)}_{\mathrm{B\text{-}B}} + 2X(1-X)\Omega^{(2)}_s\right], \tag{11}$$

TABLE I. Energetics of W-Re systems calculated with DFT. All the values from Refs. [53,54] listed in this table were also confirmed by our own calculations.

Quantity	Value	Source
$E^{\mathrm{A}}_{\mathrm{coh}}$	8.3276	This work
$E^{\mathrm{B}}_{\mathrm{coh}}$	7.4070	This work
Ω^*_s	$-0.1571 - 0.2311X$	Ref. [30]
E^{V}_f	3.1690	This work
$E^{(a)}_b$	-0.2096	This work
$E^{(b)}_b$	-0.1520	This work
$E^{(c)}_b$	-0.3079	This work
$E^{(d)}_b$	-0.2992	This work
$E^{\mathrm{V\text{-}V}}_{b,1\mathrm{nn}}$	-0.0146	This work[a]
$E^{\mathrm{V\text{-}V}}_{b,2\mathrm{nn}}$	0.3028	This work[a]
E^{AA}_f	10.16	Ref. [50]
E^{AB}_f	9.49	Ref. [50]
$E^{\mathrm{AA\text{-}B}}_{b,1\mathrm{nn}}$	-0.52	Ref. [50]
$E^{\mathrm{AB\text{-}B}}_{b,1\mathrm{nn}}$	-0.53	Ref. [53]
$E^{\mathrm{AA\text{-}AA}}_{b,1\mathrm{nn}}$	-2.12	Ref. [54]
$E^{\mathrm{AA\text{-}AB}}_{b,1\mathrm{nn}}$	-2.12	Assumed[b]
$E^{\mathrm{AB\text{-}AB}}_{b,1\mathrm{nn}}$	-3.2	Ref. [30]
$E^{\mathrm{V}\rightarrow\mathrm{A}}_m$ (A)	1.623	This work
$E^{\mathrm{V}\rightarrow\mathrm{B}}_m$ (A)	1.651	This work
$E^{\mathrm{V}\rightarrow\mathrm{A}(1)}_m$ [Fig. 3(c)]	1.7151	This work
$E^{\mathrm{V}\rightarrow\mathrm{A}(2)}_m$ [Fig. 3(c)]	1.6378	This work
$E^{\mathrm{V}\rightarrow\mathrm{B}(3)}_m$ [Fig. 3(c)]	1.577	This work
$E^{\mathrm{V}\rightarrow\mathrm{A}}_m$ (V)	1.623	This work
$E^{\mathrm{V}\rightarrow\mathrm{B}}_m$ (V)	1.651	This work

[a]These are with the xc-energy correction from Ref. [55].
[b]The only exception is the binding energy between an AA and an AB interstitial, which is assumed to be equal to the binding energy between two AA.

[4]These are with the xc-energy correction from Ref. [55].

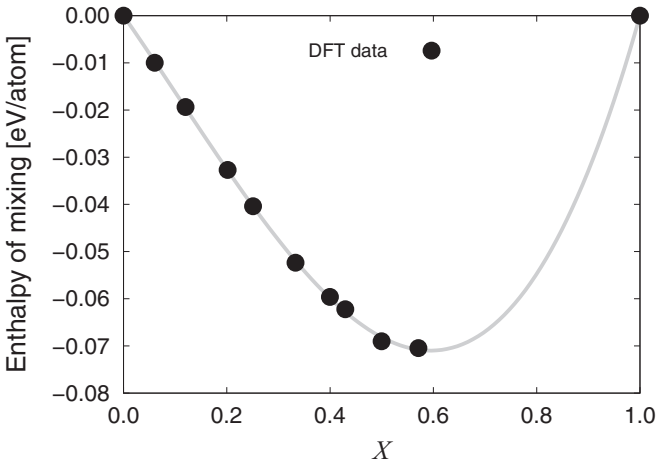

FIG. 2. Enthalpy of mixing as a function of solute concentration from Ref. [30] and third-degree polynomial fit.

where X is the global solute concentration, and Ω_s is the *heat of solution*, defined as

$$\Omega_s^{(1)} = \varepsilon_{\text{A-B}}^{(1)} - \tfrac{1}{2}\left(\varepsilon_{\text{A-A}}^{(1)} + \varepsilon_{\text{B-B}}^{(1)}\right), \tag{12}$$

$$\Omega_s^{(2)} = \varepsilon_{\text{A-B}}^{(2)} - \tfrac{1}{2}\left(\varepsilon_{\text{A-A}}^{(2)} + \varepsilon_{\text{B-B}}^{(2)}\right). \tag{13}$$

Combining Eqs. (10) and (11), ΔH^{mix} can be expressed as

$$X(1-X)\Omega_s^* = \Delta H^{\text{mix}} + (1-X)E_{\text{coh}}^{\text{A}} + XE_{\text{coh}}^{\text{B}}, \tag{14}$$

where $\Omega_s^* = z_1\Omega_s^{(1)} + z_2\Omega_s^{(2)}$. To obtain the dependence of the heat of solution on the solute concentration, we fit the left-hand side of Eq. (14) to the data points for the mixing enthalpies as a function of X calculated in our previous work [30]. The best fit, shown in Fig. 2, is achieved when Ω_s^* is expressed a linear function of the concentration:

$$\Omega_s^* = w_0 + w_1 X$$

with $w_0 = -0.1571$ and $w_1 = -0.2311$. The negative values of w_0 and w_1 suggest a moderate tendency towards ordering, which becomes larger as the solute concentration increases. Combining Eqs. (9), (10), (12), and (14), one can obtain the values of $\Omega_s^{(1)}$, $\Omega_s^{(2)}$, $\varepsilon_{\text{A-B}}^{(1)}$, and $\varepsilon_{\text{A-B}}^{(2)}$. A nonconstant Ω_s^* effectively implies that $\varepsilon_{\text{A-B}}$ is also a function of the concentration. Moreover, to reflect local composition variations in the W-Re alloys, we make the assumption that the dependence of $\varepsilon_{\text{A-B}}^{(1)}$ and $\varepsilon_{\text{A-B}}^{(2)}$ on X can be transferred to the local environment of each atom, such that both bond energy coefficients are functions of the local composition, which we term x, and must be computed on the fly for each A-B pair in the system.

2. Vacancy parameters

The vacancy bond coefficients are $\varepsilon_{\text{A-V}}$, $\varepsilon_{\text{B-V}}$, and $\varepsilon_{\text{V-V}}$. $\varepsilon_{\text{A-V}}$ can be readily obtained from the value of the vacancy formation energy:

$$E_f^{\text{V}} = E_{\text{coh}}^{\text{A}} - z_1\varepsilon_{\text{A-V}}^{(1)} - z_2\varepsilon_{\text{A-V}}^{(2)}, \tag{15}$$

where E_f^{V} is the vacancy formation energy in pure W (given in Table I). $\varepsilon_{\text{B-V}}$ can be obtained from the binding energies of

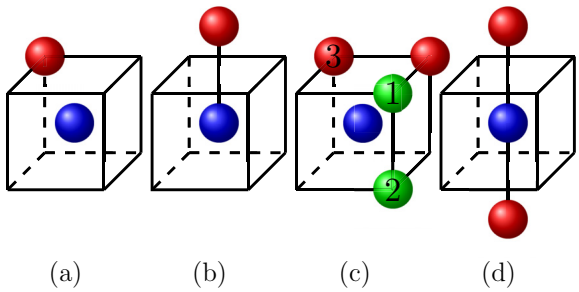

FIG. 3. Configurations of V-Re clusters used to extract bond energy coefficients $\varepsilon_{\text{A-V}}$ and $\varepsilon_{\text{B-V}}$. Blue spheres represent vacancies, red spheres represents Re atoms. All other lattice sites are occupied by A atoms, which are omitted for clarity. Green spheres indicate the various equivalent sites for atoms to exchange positions with the vacancy.

V-Re configurations, which for a structure involving m solute atoms and n vacancies is defined as

$$E_b^{\text{B}_m\text{V}_n} = E_f^{\text{B}_m\text{V}_n} - mE_f^{\text{B}} - nE_f^{\text{V}}, \tag{16}$$

where the E_f are the respective formation energies of each structure. In this work, binding energies for the four vacancy-solute configurations shown in Fig. 3 have been calculated (cf. Table I). One can now rewrite Eq. (16) as a function of the B-V bond coefficients $\varepsilon_{\text{B-V}}^{(1)}$ and $\varepsilon_{\text{B-V}}^{(2)}$ for each one of the configurations in the figure:

$$E_b^{(a)} = \varepsilon_{\text{B-V}}^{(1)} + \varepsilon_{\text{A-A}}^{(1)} - \varepsilon_{\text{A-B}}^{(1)} - \varepsilon_{\text{A-V}}^{(1)}, \tag{17a}$$

$$E_b^{(b)} = \varepsilon_{\text{B-V}}^{(2)} + \varepsilon_{\text{A-A}}^{(2)} - \varepsilon_{\text{A-B}}^{(2)} - \varepsilon_{\text{A-V}}^{(2)}, \tag{17b}$$

$$E_b^{(c)} = 2\varepsilon_{\text{B-V}}^{(1)} + \varepsilon_{\text{B-B}}^{(2)} + 2\varepsilon_{\text{A-A}}^{(1)} + \varepsilon_{\text{A-A}}^{(2)} - 2\varepsilon_{\text{A-V}}^{(1)} - 2\varepsilon_{\text{A-B}}^{(1)} - 2\varepsilon_{\text{A-B}}^{(2)} + 14\Delta\varepsilon_{\text{A-B}}^{(1)} + 10\Delta\varepsilon_{\text{A-B}}^{(2)}, \tag{17c}$$

$$E_b^{(d)} = 2\varepsilon_{\text{B-V}}^{(2)} + 2\varepsilon_{\text{A-A}}^{(2)} - 2\varepsilon_{\text{A-B}}^{(2)} - 2\varepsilon_{\text{A-V}}^{(2)}, \tag{17d}$$

where $\Delta\varepsilon_{\text{A-B}}^{(m)}$ is the change in $\varepsilon_{\text{A-B}}^{(m)}$ due to the local solute concentration change resulting from the vacancy jump.

To define the dependence on x of $\varepsilon_{\text{B-V}}^{(1)}$, we must consider two factors. First, our DFT calculations show that $\varepsilon_{\text{A-V}}^{(1)} > \varepsilon_{\text{B-V}}^{(1)}$. Second, the value of $\varepsilon_{\text{B-V}}^{(1)}$ is seen to increase with local concentration. Both of these conditions are satisfied by assuming a dependence such as $\varepsilon_{\text{B-V}}^{(1)}(x) = \varepsilon_{\text{A-V}}^{(1)} - ax^{-1}$, where a is a fitting constant. As well, $\varepsilon_{\text{B-V}}^{(2)}$ is seen to independently increase with concentration, such that $\varepsilon_{\text{B-V}}^{(2)}(x) = bx + c$, where b and c are fitting parameters.

$\varepsilon_{\text{V-V}}$ can be readily calculated by considering the binding energy of a divacancy:

$$E_{b,1\text{nn}}^{\text{V-V}} = \varepsilon_{\text{A-A}}^{(1)} + \varepsilon_{\text{V-V}}^{(1)} - 2\varepsilon_{\text{A-V}}^{(1)}, \tag{18}$$

$$E_{b,2\text{nn}}^{\text{V-V}} = \varepsilon_{\text{A-A}}^{(2)} + \varepsilon_{\text{V-V}}^{(2)} - 2\varepsilon_{\text{A-V}}^{(2)}. \tag{19}$$

It is interesting to note that, in accordance with several other studies [53,59–62], $E_{b,2\text{nn}}^{\text{V-V}}$ takes a positive value (cf. Table I), indicating repulsion between vacancies that are at 2nn distances of each other.

TABLE II. Bond energy coefficients with the equation used for their calculation, and the literature source. x is the local solute concentration.

Quantity	Value	Equation	Source
$\varepsilon^{(1)}_{\text{A-A}}$	-1.5815	Cohesive energy, Eq. (9)	This work
$\varepsilon^{(2)}_{\text{A-A}}$	-0.6672	Cohesive energy, Eq. (9)	This work
$\varepsilon^{(1)}_{\text{B-B}}$	-1.4067	Cohesive energy, Eq. (9)	This work
$\varepsilon^{(2)}_{\text{B-B}}$	-0.5935	Cohesive energy, Eq. (9)	This work
$\varepsilon^{(1)}_{\text{A-B}}$	$-1.5090-0.0219x$	Mixing energy	Ref. [30]
$\varepsilon^{(2)}_{\text{A-B}}$	$-0.6366-0.0092x$	Eq. (9)	Ref. [30]
$\varepsilon^{(1)}_{\text{A-V}}$	-0.4898	Formation energy, Eq. (9)	This work
$\varepsilon^{(2)}_{\text{A-V}}$	-0.2067	Formation energy, Eq. (9)	This work
$\varepsilon^{(1)}_{\text{B-V}}$	$-0.4898-0.009432/x$	Formation energy fitted to $\varepsilon^{(1)}_{\text{B-V}}=a+b/x$	This work
$\varepsilon^{(2)}_{\text{B-V}}$	$-0.3311+0.036x$	Formation energy fitted to $\varepsilon^{(2)}_{\text{B-V}}=a+bx$	This work
$\varepsilon^{(1)}_{\text{V-V}}$	0.5873	1nn binding energy	This work
$\varepsilon^{(2)}_{\text{V-V}}$	0.5566	2nn binding energy	This work
$\varepsilon^{(1)}_{\text{AA-A}}$	0.1740	Formation energy, Eq. (9)	Ref. [50]
$\varepsilon^{(2)}_{\text{AA-A}}$	0.0734	Formation energy, Eq. (9)	Ref. [50]
$\varepsilon^{(1)}_{\text{AB-A}}$	0.1104	Formation energy, Eq. (9)	Ref. [50]
$\varepsilon^{(2)}_{\text{AB-A}}$	0.0466	Formation energy, Eq. (9)	Ref. [50]
$\varepsilon^{(1)}_{\text{AA-B}}$	-0.2750	Binding energy	Ref. [50]
$\varepsilon^{(2)}_{\text{AA-B}}$	-0.1160	Eq. (9)	Ref. [50]
$\varepsilon^{(1)}_{\text{AB-B}}$	-0.3486	Binding energy	Ref. [53]
$\varepsilon^{(2)}_{\text{AB-B}}$	-0.1470	Eq. (9)	Ref. [53]
$\varepsilon^{(1)}_{\text{AA-AA}}$	-0.1905	Binding energy	Ref. [54]
$\varepsilon^{(2)}_{\text{AA-AA}}$	-0.0804	Eq. (9)	Ref. [54]
$\varepsilon^{(1)}_{\text{AA-AB}}$	-0.2505	Binding energy	Assumed[a]
$\varepsilon^{(2)}_{\text{AA-AB}}$	-0.1057	Eq. (9)	Assumed[a]
$\varepsilon^{(1)}_{\text{AB-AB}}$	-1.3977	Binding energy	Ref. [30]
$\varepsilon^{(2)}_{\text{AB-AB}}$	-0.5897	Eq. (9)	Ref. [30]

[a]The only exception is the binding energy between an AA and an AB interstitial, which is assumed to be equal to the binding energy between two AA.

3. *Interstitial defect parameters*

The interstitial bond coefficients include $\varepsilon_{\text{AA-A}}$, $\varepsilon_{\text{AB-A}}$, $\varepsilon_{\text{AA-B}}$, $\varepsilon_{\text{AB-B}}$, $\varepsilon_{\text{AA-AA}}$, $\varepsilon_{\text{AA-AB}}$, and $\varepsilon_{\text{AB-AB}}$. $\varepsilon_{\text{AA-A}}$ and $\varepsilon_{\text{AB-A}}$ are calculated directly from the formation energies of SIAs and mixed dumbbells:

$$E_f^{\text{AA}} = -4\varepsilon^{(1)}_{\text{A-A}} - 3\varepsilon^{(2)}_{\text{A-A}} + 8\varepsilon^{(1)}_{\text{AA-A}} + 6\varepsilon^{(2)}_{\text{AA-A}}, \quad (20)$$

$$E_f^{\text{AB}} = -4\varepsilon^{(1)}_{\text{A-A}} - 3\varepsilon^{(2)}_{\text{A-A}} + 8\varepsilon^{(1)}_{\text{AB-A}} + 6\varepsilon^{(2)}_{\text{AB-A}}. \quad (21)$$

The other bond coefficients are obtained from various binding energies:

$$E_{b,1\text{nn}}^{\text{AA-B}} = \varepsilon^{(1)}_{\text{AA-B}} + \varepsilon^{(1)}_{\text{A-A}} - \varepsilon^{(1)}_{\text{AA-A}} - \varepsilon^{(1)}_{\text{A-B}}, \quad (22)$$

$$E_{b,1\text{nn}}^{\text{AB-B}} = \varepsilon^{(1)}_{\text{AB-B}} + \varepsilon^{(1)}_{\text{A-A}} - \varepsilon^{(1)}_{\text{AB-A}} - \varepsilon^{(1)}_{\text{A-B}}, \quad (23)$$

$$E_{b,1\text{nn}}^{\text{AA-AA}} = \varepsilon^{(1)}_{\text{AA-AA}} + \varepsilon^{(1)}_{\text{A-A}} - 2\varepsilon^{(1)}_{\text{AA-A}}, \quad (24)$$

$$E_{b,1\text{nn}}^{\text{AA-AB}} = \varepsilon^{(1)}_{\text{AA-AB}} + \varepsilon^{(1)}_{\text{A-A}} - \varepsilon^{(1)}_{\text{AA-A}} - \varepsilon^{(1)}_{\text{AB-A}}, \quad (25)$$

$$E_{b,1\text{nn}}^{\text{AB-AB}} = \varepsilon^{(1)}_{\text{AB-AB}} + \varepsilon^{(1)}_{\text{A-A}} - 2\varepsilon^{(1)}_{\text{AB-A}}. \quad (26)$$

These formation and binding energies are all taken from the literature.[5]

All the bond energy coefficients, the equation used for their calculation, and the source of the numbers are compiled in Table II.

4. *Migration parameters*

The attempt frequency [ν in Eq. (6)] used for vacancy jumps in this work is set to be equal to the Debye frequency of W, or 6.5×10^{12} Hz [63], while for interstitials we use a value of 1.5×10^{12} Hz [49].

From Eq. (7), there are six different saddle-point bond coefficients: $\varepsilon^{sp(m)}_{\text{A-A}}$, $\varepsilon^{sp(m)}_{\text{A-B}}$, $\varepsilon^{sp(m)}_{\text{A-V}}$, $\varepsilon^{sp(m)}_{\text{B-A}}$, $\varepsilon^{sp(m)}_{\text{B-B}}$, and $\varepsilon^{sp(m)}_{\text{B-V}}$, where m = 1nn, 2nn. In this notation, $\varepsilon^{sp(m)}_{\alpha\text{-}\beta}$ represents the

[5]The only exception is the binding energy between an AA and an AB interstitial, which is assumed to be equal to the binding energy between two AA.

TABLE III. Saddle-point bond energy coefficients for vacancy jumps (in eV).

Quantity	Value	Quantity	Value
$\varepsilon^{sp(1)}_{\text{A-A}}$	−2.5975	$\varepsilon^{sp(2)}_{\text{A-A}}$	−0.5041
$\varepsilon^{sp(1)}_{\text{A-B}}$	−2.6451	$\varepsilon^{sp(2)}_{\text{A-B}}$	−0.5532
$\varepsilon^{sp(1)}_{\text{A-V}}$	0.5465	$\varepsilon^{sp(2)}_{\text{A-V}}$	0.1060
$\varepsilon^{sp(1)}_{\text{B-A}}$	−2.5188	$\varepsilon^{sp(2)}_{\text{B-A}}$	−0.4888
$\varepsilon^{sp(1)}_{\text{B-B}}$	−2.5417	$\varepsilon^{sp(2)}_{\text{B-B}}$	−0.4943
$\varepsilon^{sp(1)}_{\text{B-V}}$	0.2902	$\varepsilon^{sp(2)}_{\text{B-V}}$	0.0563

energy of the bond between the atom at the saddle point α and its closest lattice neighbor β. This means $\varepsilon^{sp(m)}_{\alpha\text{-}\beta} \neq \varepsilon^{sp(m)}_{\beta\text{-}\alpha}$.

The saddle-point bond coefficients connected to a lattice atom A (W atom), $\varepsilon^{sp(m)}_{\alpha\text{-A}}$, can be calculated as

$$z_1^{sp}\varepsilon^{sp(1)}_{\alpha\text{-A}} + z_2^{sp}\varepsilon^{sp(2)}_{\alpha\text{-A}} = E_m + \sum_{n,q}\varepsilon^{(n)}_{X\text{-}q} + \sum_{n,r\neq X}\varepsilon^{(n)}_{V\text{-}r}, \quad (27)$$

where z_1^{sp} and z_2^{sp} are the numbers of first- and second-nearest neighbors of an atom at the saddle point, which are both equal to 6 for the bcc lattice, and E_m is the migration energy. The term $\Delta E_{ij}^{\text{nonbroken}}$ in Eq. (7) is zero here since no solute concentration change is involved in an A-atom jump. $\varepsilon^{sp(2)}_{\alpha\text{-A}}$ is obtained from $\varepsilon^{sp(1)}_{\alpha\text{-A}}$ using Eq. (9). Vacancy bonds are calculated in a similar manner.

To calculate the saddle-point bond coefficients pertaining to B (Re) atoms, $\varepsilon^{sp(m)}_{\alpha\text{-B}}$, one must consider local solute concentration changes. To this end, we resort to the configurations shown in Fig. 3(c). The A-B saddle-point coefficients $\varepsilon^{sp(m)}_{\text{A-B}}$ are obtained from A-atom jumps, labeled "1" and "2" in Fig. 3(c), into the vacant site. The B-B saddle-point coefficient $\varepsilon^{sp(1)}_{\text{B-B}}$ is computed assuming a B-atom (labeled "3" in the figure) jump into the vacancy. Equation (9) is then used to obtain the 2nn coefficients. All the necessary DFT calculations to calculate the saddle-point bond coefficients were performed as part of the present work, and are given in Table III.

The migration energies of SIA and mixed interstitials, the activation energy for SIA rotation, as well as the correlation factors at different temperatures are taken from the literature, and listed in Table IV.

5. *DFT calculations*

Density functional theory calculations were carried out using the projector augmented wave (PAW) method [64,65] as implemented in the Vienna *ab initio* simulation package [66–69]. Since interstitial configurations involve short interatomic distances "hard" PAW setups that include semicore electron states were employed with a plane wave energy cutoff of 300 eV.

Exchange and correlation effects were described using the generalized gradient approximation [70] while the occupation of electronic states was performed using the first-order Methfessel-Paxton scheme with a smearing width of 0.2 eV. The Brillouin zone was sampled using $5 \times 5 \times 5$ $\vec{k}$-point grids. (A detailed discussion of the effect of different computational parameters on the results can be found in Ref. [50].) All structures were optimized allowing full relaxation of both ionic positions and cell shape with forces converged to below 10 meV/Å. Migration barriers were computed using $4 \times 4 \times 4$ supercells and the climbing image-nudged elastic band method with three images [71].

TABLE IV. Self-interstitial migration parameters. The jump distance for SIA migration is $\delta = a_0\sqrt{3}/2$.

Quantity	Value	Source
E_m^{AA}	0.003	Ref. [28]
E_r^{AA}	0.43	Ref. [28]
E_m^{AB}	0.12	Ref. [30]
f	$2.93 - 0.00055T$	Ref. [49]

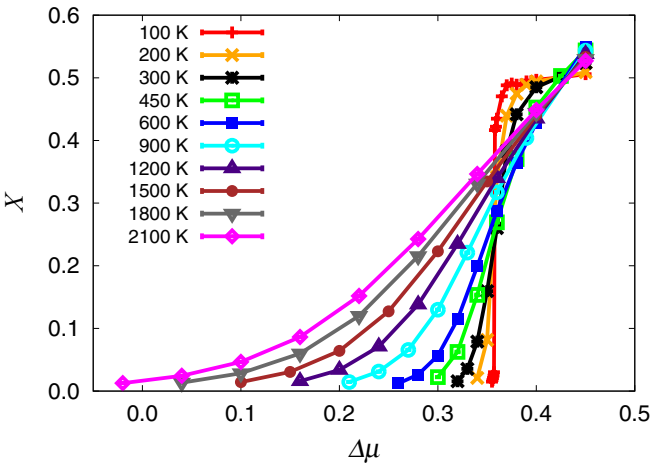

FIG. 4. Solute composition X as a function of chemical potential $\Delta\mu$ at different temperatures.

III. RESULTS

A. Structural phase diagrams

Although our energy model includes thermodynamic information reflective of the phase stability of W-Re alloys, the model consists of a rigid lattice with bcc structure and is thus suitable only for a given, well-defined, concentration range. Our DFT calculations yield bond energies that are consistent with a stable binary alloy from zero to approximately 40 at.% Re [30]. This is confirmed by way of SGMC simulations performed as a function of composition and temperature in $64 \times 64 \times 64$ computational cells. Figure 4 shows the set of stable compositions obtained as a function of the chemical potential for several temperatures.

The figure shows a clear jump in the Re concentration at a temperature of approximately 100 K. This is indicative of a phase transformation, which results in phase-separated structures at temperatures at or below approximately 200 K in the $0.0 < X < 0.5$ concentration range. In Appendix A we discuss this phase-separated system in more detail, characterized by precipitation of B2 clusters in the bcc lattice. For now, to characterize the configurations obtained, we calculate their short-range order (SRO) according to the Warren-Cowley

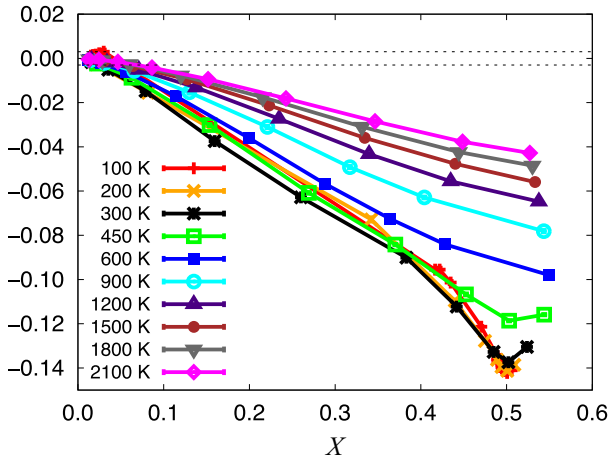

FIG. 5. Short-range-order parameter η as a function of global solute composition X at different temperatures. The dashed line indicates the SRO interval caused by normal concentration fluctuations during the generation of atomistic samples.

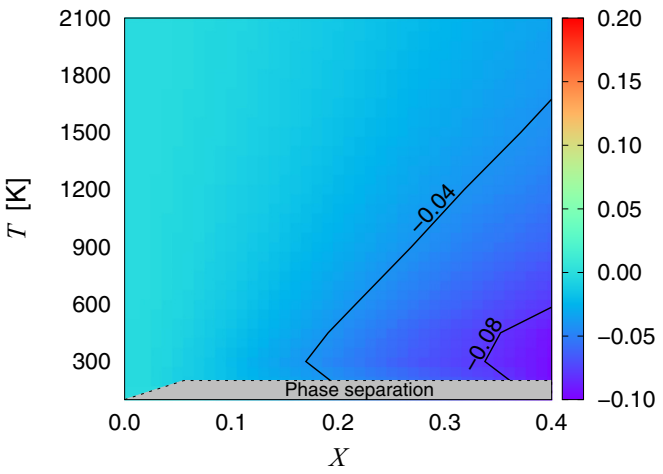

FIG. 6. Structural phase diagram showing regions of changing SRO. The dashed lines are the limits of applicability of the rigid bcc lattice model. The system displays slightly negative SRO throughout the entire temperature-concentration space, indicating a preference to be in a solid solution state. The gray band at low temperatures signifies the region of coexistence of the bcc and B2 phases (see Appendix A).

parameter [72]:

$$\eta = N_B^{-1} \sum_i^{N_B} \left(1 - \frac{x_i(\mathrm{A})}{1 - X}\right), \tag{28}$$

which gives the SRO parameter η of Re atoms with respect to matrix W atoms, with $x_i(\mathrm{A})$ being the fraction of A atoms surrounding each solute atom i. The sum extends to all B atoms in the system.

According to this definition, $\eta > 0$ implies phase separation, $\eta = 0$ represents an ideal solid solution, and $\eta < 0$ indicates ordering. However, the SRO parameter of a random solution has a range of ± 0.003 regardless of solute composition due to the random occurrence of dimers, trimers, and other small clusters. This band of *natural* order is marked with dashed lines in Fig. 5, which shows the equilibrium SRO as a function of X for several temperatures. As the figure shows, the SRO parameter is near zero for dilute systems, and gradually becomes negative as the concentration increases. The corresponding T-X phase diagram is provided in Fig. 6.

The equilibrium structures of the ordered compounds observed primarily at lower temperatures and higher concentrations are analyzed in Appendix A. At high temperatures and lower Re concentrations, the system behaves like a random solid solution for all practical purposes.

1. Effect of vacancies on phase diagram

It is well known that nonequilibrium concentrations of defects can alter the thermodynamic behavior of an alloy. For the W-Re system, Wrobel *et al.* have studied the ternary W-Re-vacancy system and found that Re clustering occurs in the presence of nonthermodynamic vacancy concentrations [21]. Although these are unrealistic homogeneous defect concentrations, we can justify their study to hint at what could happen in highly heterogeneous situations, such as near defect sinks in irradiated materials. Clusters appear as semiordered structures of alternating solute and vacancy planes—a necessity given the short-range repulsion between Re atoms on the one hand and vacancies on the other (cf. Table I). Next, we carry out a similar study involving various vacancy concentrations, temperatures, and solute concentrations to obtain structural phase diagrams such as that shown in Fig. 6. Each configuration is optimized by combining SGMC steps with energy minimization steps following the process described in Sec. II C. Figure 7 shows the diagrams for vacancy concentrations of $C_v = 0.01, 0.1, 0.2, 0.5$ at.% using $64 \times 64 \times 64$ primitive cells.

As a representative example, Fig. 8(a) shows the equilibrated configuration at 600 K, 1.8 at.% Re (which occurs for $\Delta\mu = 0.26$), and $C_v = 0.5$ at.%. The figure shows several Re-vacancy clusters with an ordered structure, consistent with the study by Wrobel *et al.* [21]. Due to their ordered structure, these solute-vacancy clusters form only at Re concentrations that are commensurate with the vacancy concentration in the system, i.e., at values of $X \lesssim 0.04$ in most cases.

2. Effect of interstitial defects on the phase diagram:

Although vacancy concentrations such as those considered in this section are several orders of magnitude larger than the vacancy concentration in thermal equilibrium, one can expect such numbers under far-from-equilibrium conditions such as under high-dose or high-dose-rate irradiation. The case is much more difficult to make for SIAs due to their much higher formation energy (3.2 vs 10.2 eV, to take two representative numbers [50]). However, given the inclination of single interstitials to convert into mixed dumbbells in the presence of solute, it is of interest to repeat the same exercise of looking at the clustering propensity of Re in such cases. The results are shown in Fig. 9 for a defect

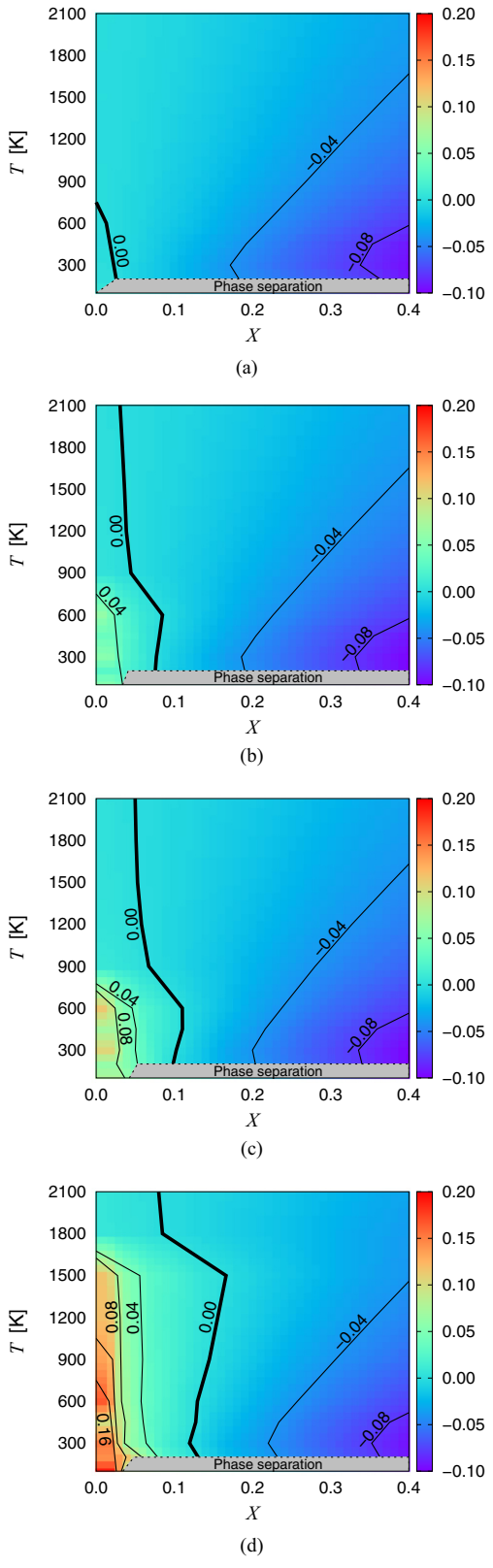

FIG. 7. Structural phase diagrams for four different vacancy concentrations. (a) $C_v = 0.01$ at.%. (b) $C_v = 0.1$ at.%. (c) $C_v = 0.2$ at.%. (d) $C_v = 0.5$ at.%. The diagrams clearly show the emergence of regions of solute segregation, characterized by positive SRO and a shifting of the transition phase boundary, $\eta = 0$, towards the right (higher concentrations).

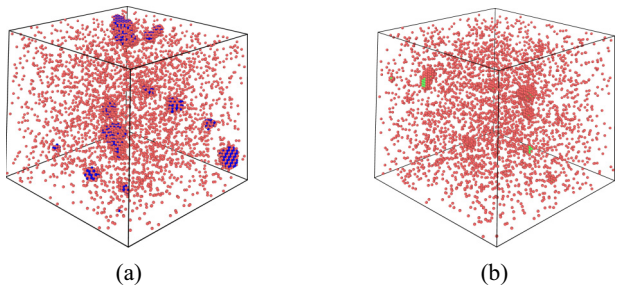

FIG. 8. Equilibrated configurations for W-Re alloys containing different defect concentrations at 600 K. (a) W–1.8 at.% Re alloy, 0.5 at.% vacancy concentration. (b) W–1.4 at.% Re alloy, 0.1 at.% mixed interstitials. Red spheres represent Re atoms; colored blue or green ones represent the defect in each case.

concentration of 0.1 at.%. The diagram reveals a stronger clustering tendency when interstitials are present compared to vacancies. Such an effect originates from both more attractive binding energies between mixed interstitials and solute atoms, and between mixed interstitials with themselves. A snapshot of the equilibrated atomistic configuration is shown in Fig. 8(b), where the precipitates are seen to form platelet-like structures with a mixed dumbbell core surrounded by substitutional solute atoms.

B. Kinetic evolution of irradiated W-Re alloys

There are a number of factors that call for performing kMC simulations in W-Re systems:

(1) First, equilibrium Monte Carlo calculations such as those performed in Sec. III A do not provide information about the precipitate nucleation and growth mechanisms, as well as the time scales involved.

(2) Second, there is clear experimental evidence of Re-cluster formation in the absence of vacancies. Hasegawa *et al.* [9,73] and Hu *et al.* [10] have both reported the formation of W-Re intermetallic precipitates after high-dose, fast neutron

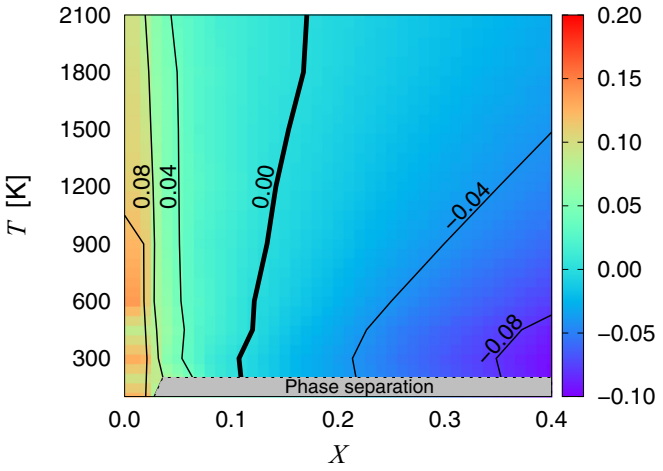

FIG. 9. Structural phase diagram for 0.1 at.% mixed-dumbbell concentration. The diagram shows the emergence of regions of solute segregation, characterized by $\eta > 0$, up to $X = 0.1\%$.

irradiation. Moreover, recent irradiation experiments have revealed the formation of Re-rich clusters with bcc structure, i.e., prior to their conversion into σ and/or χ precipitates. For example, Klimenkov *et al.* note that Re-rich particles not associated with cavities formed in neutron-irradiated single-crystal W [22]. As well, using atom-probe tomography Xu *et al.* have performed detailed analyses of Re-rich atmospheres in bcc W without detecting significant numbers of vacancies [14].

(3) New understanding regarding interstitial-mediated solute transport in W-Re alloys [29,30], together with the results in Sec. III A 2, call for renewed simulation efforts incorporating these new mechanisms—in particular, the three-dimensional and associative nature of Re transport via mixed-dumbbell diffusion.

These considerations motivate the following study of the Re precipitation kinetics under irradiation conditions. First, however, we proceed to calculate diffusion coefficients and transport coefficients for defect species and solute atoms.

1. Calculation of diffusion coefficients

Tracer diffusion coefficients (i.e., in the absence of a concentration gradient) for vacancies, interstitials, and solute species in three dimensions are assumed to follow an Arrhenius temperature dependence:

$$D(T) = \nu f \delta^2 \exp\left(-\frac{E_a}{kT}\right), \tag{29}$$

where ν is the so-called *attempt* frequency, f is the correlation factor, δ is the jump distance, E_a is the activation energy, and $D_0 = \nu f \delta^2$ is the diffusion prefactor. Defect diffusivities can be obtained directly from this equation, with $E_a \equiv E_m$. For solute diffusion via the vacancy mechanism, the above expression must be multiplied times the probability of finding a vacancy in one of the 1nn positions, such that $D_0 = z_1 \nu f \delta^2$ and $E_a = E_m + E_f^{\mathrm{V}}$. However, fluctuations in local chemistry prevent us from using equations for homogeneous systems such as Eq. (29) to calculate the diffusivities of solutes and vacancies as a function of the global solute concentration. In such cases, diffusion coefficients must be obtained by recourse to Einstein's equation:

$$D = \frac{\langle \Delta r^2 \rangle}{6\Delta t}, \tag{30}$$

where $\langle \Delta r^2 \rangle$ is the mean-squared displacement (msd) and Δt is the time interval. This formula assumes equilibrium defect concentrations, which are generally several orders of magnitude smaller than what a typical simulation cell can afford. For this reason, the time in Eq. (30) is not directly the time clocked in the kMC simulations, Δt_{kMC}. Rather, it must be rescaled by a coefficient that accounts for the difference in defect concentration [74,75]:

$$\Delta t = \Delta t_{\mathrm{kMC}} \frac{C^{\mathrm{kMC}}}{C^{\mathrm{eq}}}, \tag{31}$$

where C^{kMC} and C^{eq} are the defect concentrations in the kMC simulations and in equilibrium, respectively. For simulations involving only one defect, C^{kMC} is simply equal to the inverse of the number of atoms in the computational cell, $C^{\mathrm{kMC}} = N^{-1}$, while $C^{\mathrm{eq}} = \exp(-E_f/k_B T)$, where E_f is the *instantaneous* defect formation energy, i.e., calculated accounting for the local chemical environment. This is the approach used for vacancy mediated diffusion, with $E_f^{\mathrm{V}} = \sum_i \varepsilon_{\mathrm{V}\text{-}\alpha_i}$, where α_i symbolizes the neighboring atoms forming a bond with the vacancy. During simulations of solute and vacancy diffusion, E_f^{V} is updated in every Monte Carlo time step and time rescaling is performed on the fly. The starting configuration for all calculations involving solute atoms is the equilibrated alloy as obtained in Sec. III A using SGMC simulations. The results for the vacancy and solute diffusivities, D_{v} and D_{s}, can be seen in Fig. 10, while the parameters resulting from fitting the data points in the above figures to Eq. (29) are collected in Table V. While D_{v} displays a moderate dependence on the solute concentration, D_{s} is quite insensitive to it.

As discussed in Sec. II E 4, self-interstitial migration occurs by way of fast sequences of ⟨111⟩ transitions punctuated by sporadic rotations, whereas mixed dumbbell diffusion occurs via random ⟨100⟩ hops in three dimensions. Interstitial diffusivities of both types can be calculated straightforwardly by using Eq. (29) parametrized with the data in Table IV.

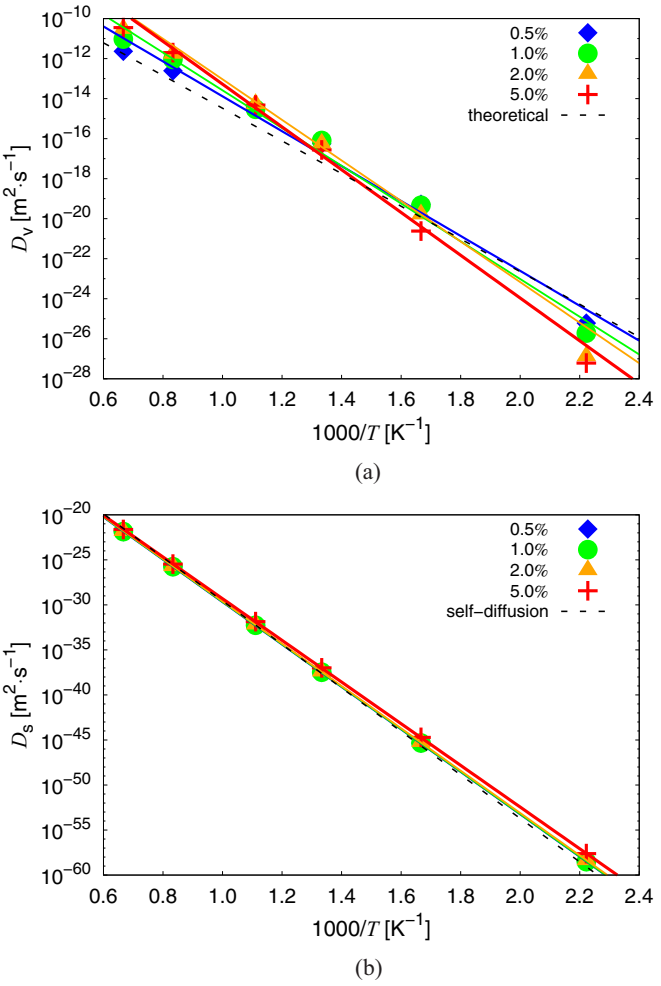

FIG. 10. Diffusivities of vacancies and solute atoms as a function of temperature and alloy concentration. (a) Vacancy diffusion. (b) Solute diffusion. The solid lines correspond to the Arrhenius fits shown in Table V, while the dashed line corresponds to Eq. (29).

TABLE V. Diffusion parameters for vacancy and solute diffusion as a function of solute concentration.

X (at.%)	D_0 (m^2 s^{-1})	E_m (eV)
	Vacancy diffusion	
0.0 [Eq. (29)]	4.84×10^{-7}	1.62
0.5	6.86×10^{-6}	1.73
1.0	6.92×10^{-5}	1.87
2.0	1.26×10^{-3}	2.08
5.0	2.57×10^{-3}	2.16
	Solute diffusion	
0.0 [Eq. (29)]	3.87×10^{-6}	$1.62 + 3.17 = 4.79$
0.5	7.56×10^{-7}	4.67
1.0	7.80×10^{-7}	4.67
2.0	7.89×10^{-7}	4.66
5.0	6.75×10^{-7}	4.59

2. *Calculation of transport coefficients*

Within linear response theory, mass transport can be related to chemical potential gradients via Onsager's phenomenological coefficients. The value and sign of these transport coefficients can provide important physical information about the nature of solute and defect fluxes. On a discrete lattice, the transport coefficients L_{ij} coupling two diffusing species can be calculated as [44,76]

$$L_{ij} = \frac{1}{6V} \frac{\langle \Delta r_i \Delta r_j \rangle}{\Delta t}, \tag{32}$$

where V is the total volume of the system, Δr_i is the total displacement of species i, and Δt is the rescaled time. Here we focus on the relationship between solutes and solutes, and solute atoms and vacancies, $L_{\text{B-B}}$ and $L_{\text{B-V}}$, as a function of temperature and Re content. Due to the associative transport mechanism of AB interstitials, the corresponding transport coefficient relating interstitials with solute atoms is always positive and we obviate its calculation. Figure 11(a) shows the results for $L_{\text{B-B}}$, which displays an Arrhenius temperature dependence and is always positive. The dependence on solute concentration is not significant up to 5%, with an average activation energy of 4.7 eV—very similar to the solute diffusion activation energy—and a prefactor of approximately 3.9×10^{20} m^{-1} s^{-1}. $L_{\text{B-B}}$ is by definition related to the solute diffusion coefficient presented above.

In Fig. 11(b) we plot the ratio $L_{\text{B-V}}/L_{\text{B-B}}$. Two observations stand out directly from the figure. First, the value of $L_{\text{B-V}}$ is always negative (the exception being at 450 K, when it is almost zero). This indicates a reverse coupling between solutes and vacancies; i.e., vacancy fluxes oppose solute fluxes. The implications of this calculation will become clearer when we study solute precipitation in the next section. Second, $L_{\text{B-V}}$ is on average about an order of magnitude larger (in absolute value) than $L_{\text{B-B}}$, which is to be expected for substitutional solutes moving by a vacancy mechanism.

Finally, we have looked at the ratio $L_{\text{B-V}}/L_{\text{A-V}}$. The values are generally positive, albeit quite small, indicating that both atomic fluxes are weakly aligned. However, transport coefficients are not normalized on a per atom basis, which gives the impression that B-V transport is of smaller magnitude than A-V transport. This is however misleading, given the large concentration difference between solvent and solute atoms. Therefore, in Fig. 11(c) we plot the $\tilde{L}_{\text{B-V}}/\tilde{L}_{\text{A-V}}$ ratio, where the tilde indicates per atom. It is clear from the figure that B atoms undergo a much faster vacancy-mediated transport than A atoms, which is consistent with a thermodynamic tendency to mixing for the unirradiated condition.

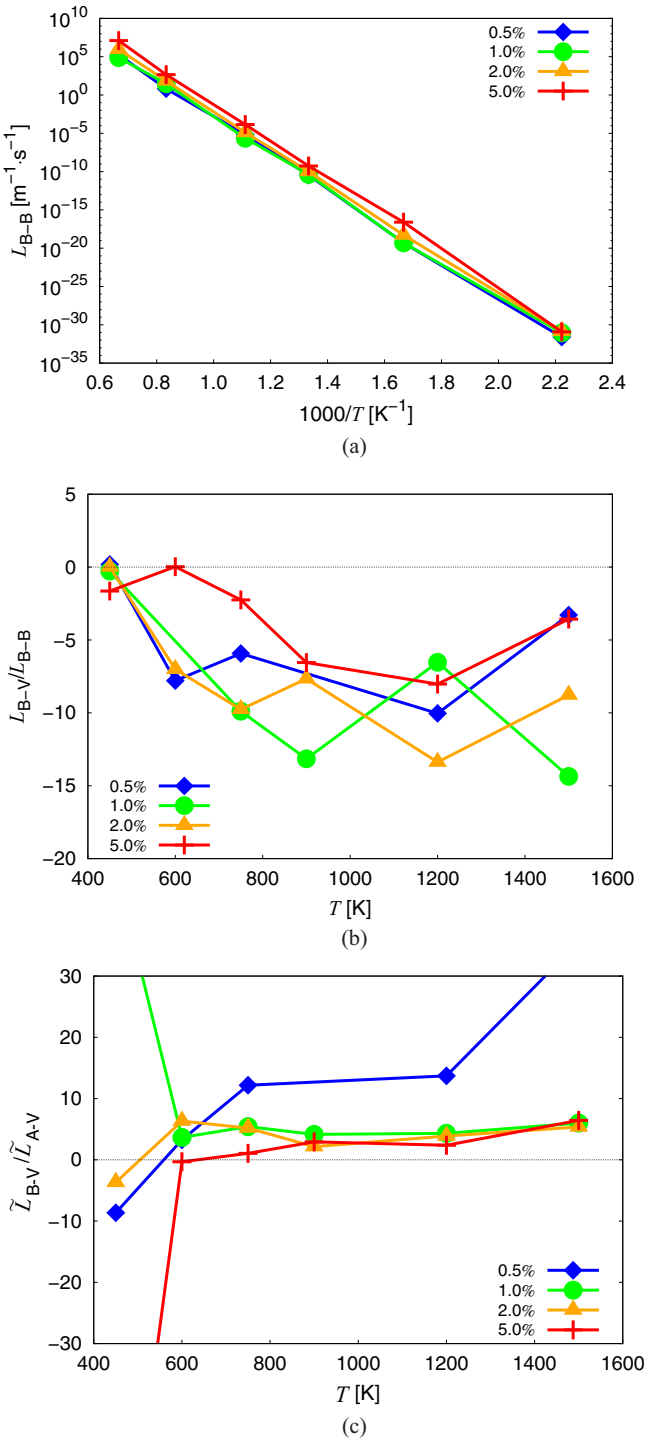

FIG. 11. Phenomenological transport coefficients for solute-solute, vacancy-solute, and solvent-solute interactions. (a) Solute-solute transport coefficient. (b) Solute-vacancy transport coefficient. (c) Relation of transport coefficients for solute-vacancy and solvent-vacancy interactions.

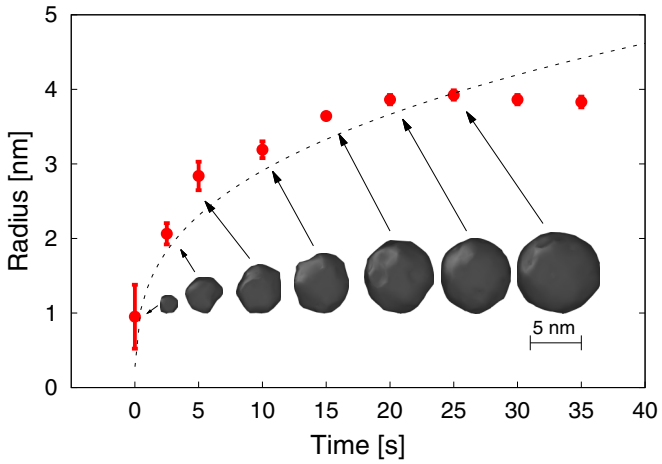

FIG. 12. Precipitate growth with time at 1800 K and 10^{-3} dpa s^{-1} in a W–2.0 at.% Re alloy. The dashed line represents perfect spherical growth (cf. Appendix B). A surface reconstruction rendition of one precipitate at various times is provided in the inset.

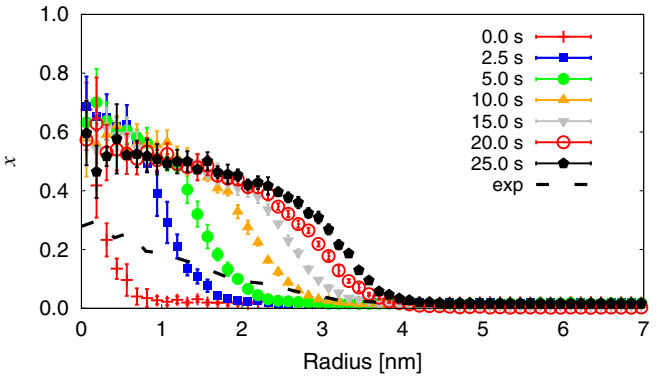

FIG. 13. Radial concentration profile as a function of time for the precipitates formed in the kMC simulations. The experimental results are taken from the work by Xu *et al.* [14].

3. *Kinetic Monte Carlo simulations*

To narrow down the large parametric space associated with irradiation of W-Re alloys (Re concentration, temperature, dose, dose rate, etc.), we resort to the study performed in Secs. III A and III A 1. It was seen there that segregation occurs most favorably at low solute compositions. For this reason, and to enable comparison with the work by Xu *et al.* [13,14], we choose a W-2Re (at.%) alloy for our study. By way of reference, this would correspond to the transmutation fraction attained after a dose of 12 dpa or 4 full-power years in DEMO's first wall according to Gilbert and Sublet [5]. When relatively high concentrations of defects are present—as one might expect during irradiation—precipitation is also favored at high temperatures, so here we carry out our simulations between 1700 and 2000 K. This corresponds to the shaded band in Fig. 1, where dots are shown marking the 2% concentration point. As the figure shows, the simulation conditions are well within the solid solubility region of W-Re, where no precipitation is expected. We use box sizes of 64^3 and 80^3 with a damage insertion rate of 10^{-3} dpa per second. As shown in Appendix B, the equivalence relation that exists between both box sizes enables us to compare them directly. Eight independent simulations were conducted for statistical averaging and stochastic error estimation.

It is seen that, on average, a precipitate starts to grow after a waiting time of $\approx$13.5($\pm$8.5) seconds (or $\approx$0.02 dpa). This time can be regarded as the average *incubation* time for the conditions considered in the study. Of course, this time does not necessarily correspond to the *nucleation* time in the thermodynamic sense, given the length and time scale limitations in our simulations. Figure 12 shows the mean size from all eight cases as a function of *growth* time, i.e., initializing the clock after the cluster nuclei are formed regardless of the observed incubation time. The dashed line in the figure is the associated spherical growth trend, which the precipitates are seen to follow for approximately 20 s. Subsequently, growth stops at a saturation radius of 4 nm, which is seen to be the stable precipitate size. In the thermodynamic limit, the solute agglomerates into one single precipitate. However, in simulations, this size is limited by the simulation box dimensions. Therefore, the value of 4 nm for the cluster radius found here has no real physical significance, and we take it to be simply associated with the computational cell employed here. A surface reconstruction rendition of one of the precipitates is also provided in the figure as a function of time. This depiction as a compact convex shape is not intended to represent the true diffuse nature of the cluster, and is only shown as an indication of the cluster average size and shape.

The next question we address is the solute concentration inside the precipitate. Xu *et al.* [13,14] have performed detailed atom probe analyses of radial concentration profiles at 573 and 773 K and find that the precipitates that form might be better characterized as "solute clouds," reaching concentrations of around 30% in the center gradually declining as the radius increases. Our analysis is shown in Fig. 13, with results averaged over the 8 cases tried here. The figure shows that the concentration at the precipitate core (within the inner 1.5 nanometers) surpasses 50%—the thermodynamic limit for the formation of intermetallic phases—which could provide the driving force for such a transformation. Because our energy model is not valid above the solid solution regime, we limit the interpretation of such phenomenon, however. What is clear is that the precipitates are not fully dense, even near their center. In fact, the relative solute concentration appears to diminish near the precipitate core once the saturation point has been reached.

Finally, we address the issue of whether it is vacancy or interstitial mediated transport that is primarily responsible for solute agglomeration and the formation of Re-rich clusters. To this end, we track the evolution with time of the incremental SRO change brought about by any given kMC event during the formation stage of one the precipitates discussed above. The results are given in Fig. 14, where contributions from SIA and mixed-interstitial jumps, vacancy jumps, and Frenkel pair insertion are plotted. These results conclusively demonstrate that mixed-interstitial transport is dominant among all other events to bring solute together. Vacancies, on the other hand, serve a dual purpose. They first act as a "hinge" between solute atoms that would otherwise repel, much in the manner shown in Fig. 8(a). This results in an initial positive contribution to the SRO, as shown in the inset to Fig. 14, by forming dimers, trimers, or other small solute clusters. However, once

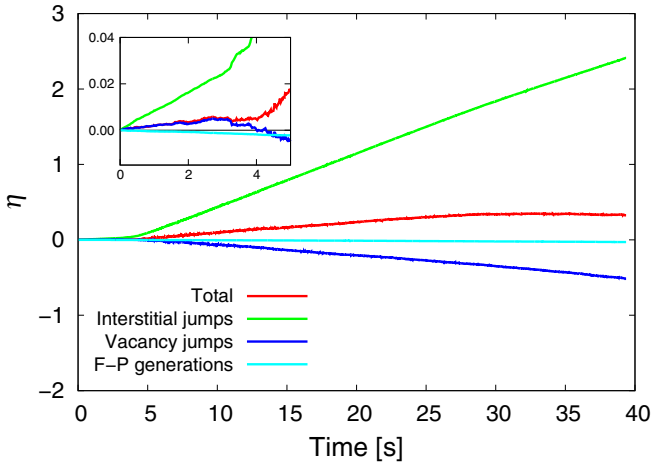

FIG. 14. Evolution of the differential SRO during the nucleation and growth in the kMC simulations.

a critical nucleus forms and starts to grow, vacancies reverse this behavior and act to dissolve the precipitate (differential SRO turns negative in Fig. 14), mostly by making the precipitate/matrix interface more diffuse. As expected, Frenkel pair insertion has practically no effect on the overall precipitate evolution.

The precipitate grows by a sustained capture of mixed interstitials and subsequent attraction of vacancies. This gives rise to localized recombination at the precipitate, which makes the precipitates incorporate solute atoms over time. Figure 15 shows the spatial location of the recombination events during a period of 2.0 s before, during, and after precipitate growth. The figure clearly shows that, once formed, the precipitate becomes a preferential site for recombinations, which results in further growth and eventually in saturation. Because the primary source of solute is via interstitial transport, which also brings W atoms, the precipitates are never fully compact ($x \sim 1$). Instead, maximum concentrations of around 50% are seen near the center when the precipitates reach their saturation size of 4-nm radius. As we will discuss in the next section, this is consistent with experimental measurements and observations of both coherent bcc clusters and incoherent σ and χ phases. As further evidence of the necessity of irradiation to sustain precipitate formation and growth, we have "relaxed" Re cluster configurations formed under irradiation by turning off defect insertion and letting the system evolve under the action of one isolated vacancy. Indeed, the system returns to a solid solution as described by the corresponding SRO at the corresponding temperature and solute concentration. One example of such relaxations is given in Fig. S2 in the Supplemental Material [77].

Simulations performed with defect sinks in the same temperature range simply result in solute segregation in the manner described in our previous work [31]. Radiation-induced precipitation results from the onset of defect fluxes to the sinks, providing sufficient competition to delay the formation of bulk precipitates beyond the time scales coverable in our kMC simulations. More information is also provided in the Supplemental Material [77].

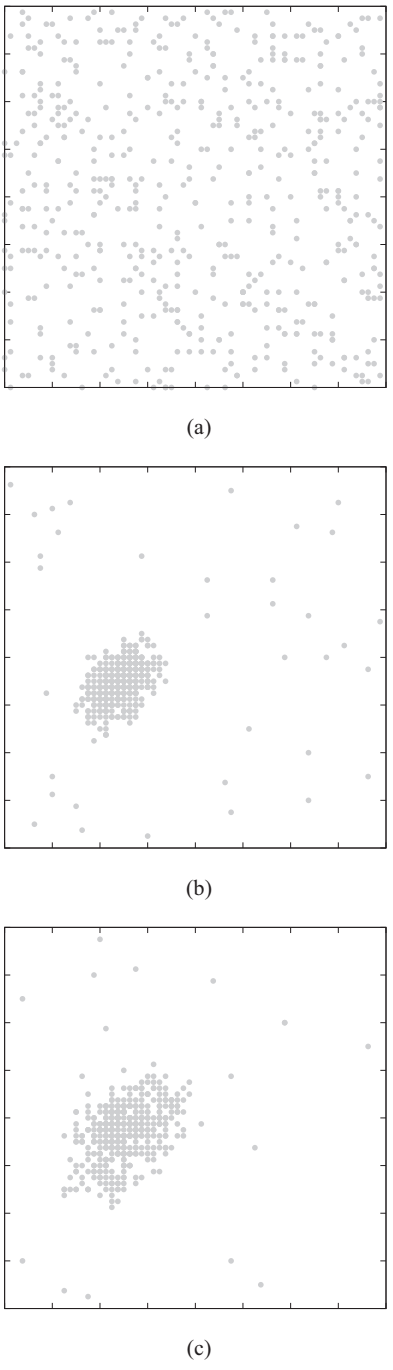

FIG. 15. Spatial distribution of recombination events for several stages of precipitate evolution. (a) During cluster nucleation. (b) During precipitate growth. (c) After size saturation.

IV. DISCUSSION AND CONCLUSIONS

A. Mechanism of nucleation and growth

On the basis of our results, the sequence of events that leads to the formation of Re-rich precipitates in irradiated W-2Re (at.%) alloys is as follows:

(1) First, a Frenkel pair is inserted in the computational box following the procedure specified in Sec. II D. As interstitials enter the system, they perform a one-dimensional migration until they encounter a solute atom, after which they become

mixed AB dumbbells capable of transporting solute in 3D. As these mixed dumbbells diffuse throughout the lattice, they encounter substitutional solute atoms and become trapped forming a B-AB complex with a binding energy of 0.15 eV (cf. Table I).

(2) The vacancy in the Frenkel pair migrates throughout the lattice contributing to the formation of small Re complexes (dimers, trimers, tetramers, etc.). Vacancy motion does not necessarily imply solute drag, as indicated by the negative value of transport coefficients in Sec. III B 2. However, as the evidence from the Metropolis Monte Carlo simulations in Fig. 7 suggests, they can form small complexes of stable Re-V clusters.

(3) The vacancy can become locally trapped in the small Re-V complexes mentioned above. However, at the high temperatures considered here, it is likely to de-trap and continue migrating until it finds the immobilized interstitial from (1), as this provides the largest thermodynamic driving force to reduce the energy of the crystal. When the vacancy and the interstitial meet, another small Re cluster is formed. Throughout this process, both mixed interstitial and vacancy hops are characterized by an increasing differential SRO parameter (cf. Fig. 14).

(4) Eventually, one of these Re clusters grows larger than the rest due to natural fluctuations. When that happens, this larger cluster has a higher likelihood of attracting the next V-AB recombination event. This signals the onset of the growth process, fueled by continued attraction of AB mixed dumbbells and the subsequent associated recombination. At this stage, vacancies reverse their role as solute-atom "hinges" and begin to contribute to cluster dissolution (negative differential SRO parameter in Fig. 14). This results in the development of a more or less diffuse interface as the precipitate grows, which delays the next recombination event and slows down growth.

(5) Although the precipitate continues to be the main pole of attraction for vacancy-interstitial recombinations (cf. Fig. 15), the system reaches a point where most of the solute is consumed into a diffuse precipitate that halts further growth. Vacancies then have more time to interact with the interface atoms before the next recombination event, which results in a smearing of the precipitate interface. In the absence of sinks, or other precipitates, the existing cluster is the sole focus of solute agglomeration, which allows it grow to its maximum size for the current alloy content of 2% Re and computational cell used (cf. Sec. III B 3). It is to be expected that with competing solute sinks in a statistically significant computational volume, the precipitates will be smaller and/or less solute-dense internally.

This qualitative explanation is built on direct evidence and interpretation from our results, described in detail in Sec. III. However, to support some of the above points more explicitly, we provide additional details in the Supplemental Material [77].

Interestingly, the essential features of our mechanism were originally proposed by Herschitz and Seidman [26,27] on the basis of atom probe observations of neutron-irradiated W-25Re alloys. Remarkably, these authors had the intuition to propose the basic ingredients needed to have Re precipitate formation identified in our work with the significantly more limited understanding available at the time.

B. Brief discussion on the validity of our results

With the computational resources available to us, we can reasonably simulate systems with less than 500 000 atoms into time scales of tens of seconds. This has proven sufficient to study Re clustering at high temperatures, where vacancy mobility is high and comparable to mixed-interstitial mobility. Recall from the previous section that the formation of clusters is predicated on the concerted action of both defect species, with mixed interstitials becoming trapped at small Re clusters followed by a recombination with a vacancy that makes the cluster grow over time. Clustering and precipitation of Re in irradiated W has been seen at temperatures sensibly lower than those explored here, such as 573 and 773 K for ion-irradiated W-Re [13,14,78], 773 and 1073 K for neutron-irradiated W in HFIR [10], 1173 K in neutron-irradiated W in the HFR reactor [22], and by Williams *et al.* at 973 $\sim$ 1173 K in EBR-II [25]. The work by Hasegawa *et al.* in JOYO [9,79] does cover—by contrast—a similar temperature range as ours. Whether the mechanism proposed here can be conceivably extended to lower temperatures with just a time scale adjustment remains to be seen. An indirect way to study temperature effects is to vary the values of the migration and binding energies that are in the Boltzmann exponentials for the transition rates. In Sec. VI, we analyze the sensitivity of the incubation time, cluster growth rates, and vacancy-Re clustering to two key parameters to shed some light on these effects.

Another intrinsic limitation of our model is that it is based on a rigid bcc lattice and cannot thus capture the transition of precipitates to the intermetallic phase. As such, our model does not necessarily reflect the true microstructural state when the local concentration surpasses 40% $\sim$ 50%, which is when σ and χ precipitates are seen to develop according to the phase diagram [15]. However, in controlled ion irradiation experiments [13,14,78] there is clear evidence that the precursors to the formation of these intermetallic precipitates are noncompact Re-rich clusters with bcc structure. We cannot but speculate how the transition from these solute-rich clusters to well-defined line compounds σ and χ takes place (perhaps via a martensitic transformation, as in Fe-Cu systems [80]), but it is clear that it is preceded by the nucleation and growth of coherent Re clusters. In our simulations, we find that the clusters have a maximum concentration of $\approx$50% in the center, in contrast with Xu *et al.*, who observe concentrations no larger than 30%. This disparity may simply be a consequence of the different temperatures considered relative to our simulations (773 vs 1800 K), as it is expected that the accumulation of solute by the mechanism proposed here will be accelerated by temperature. Regarding the size of the clusters, it is well known that in small-scale simulations such as these all the solute tends to accumulate into a single cluster. Therefore, the final cluster size depends on solute concentration and computational cell dimensions, and what we measure here is thus not physically meaningful in relation to experiments.

As well, our Re clustering mechanism is predicated on the insertion of Frenkel pairs, when it is well known that fast neutron and heavy-ion irradiation generally result in the formation of clusters of vacancies and interstitials directly in dense displacement cascades. However, even here tungsten is somewhat of a special case. Recent work [81–83] suggests that most of the defects in high-energy (>150 keV) cascades in W

appear in the form of isolated vacancies and interstitials. This, together with the fact that most displacement cascades for nonfusion neutrons and heavy ions have energies well below the 150-keV baseline, gives us confidence that our mechanism would be operative even in such scenarios.

C. Implications of our study

Beyond the obvious interest behind understanding the kinetics of Re-cluster formation in irradiated W-Re alloys, our model is useful to interpret other physical phenomena. For example, it is well known that swelling is suppressed in irradiated W-Re alloys compared to pure W [23]. By providing enhanced avenues for interstitial-vacancy recombination, small Re clusters capture mixed interstitials, allowing sufficient time for vacancies to find them and suppressing or delaying the onset of swelling. Intrinsic 3D mobility of mixed dumbbells is likely to favor recombination as well. However, we do not discard a mechanism for swelling suppression similar to that proposed for Fe-Cr alloys, where 1D migration of SIAs is restrained by Cr atoms [84]. This could conceivably occur in W-Re systems, with Re atoms and small Re clusters trapping SIA clusters and hindering their one-dimensional escape.

The mechanisms proposed here refer to homogeneous nucleation; i.e., Re clustering occurs without any assistance from RED or RIP, and hence without the need for defect sinks. This is again a remarkable feature of these alloys, confirmed by several studies [14,22,27]. As noted by Herschitz and Seidman, "The coherent precipitates were not associated with either linear or planar defects or with any impurity atoms; i.e., a true homogeneous radiation-induced precipitation occurs in this alloy," or by Klimenkov *et al.*, "The formation of Re-rich particles with a round shape was detected in the single-crystal material. These particles were formed independently of cavities." We leave out heterogeneous precipitation at voids, as the evidence in the literature is conflicting at this stage: discounted in some works [14,27] and observed in others [22].

D. Sensitivity of results to model uncertainties

The issue of sensitivity of *mesoscale* models to atomistic parameters is of course of extraordinary importance and the subject of the field of uncertainty quantification (UQ). This is especially true in a case like ours, where properties evaluated at the atomic/molecular scale are transferred to the mesoscopic scale. As it relates to this work, sources of uncertainty may originate in numerical uncertainty, model uncertainty, and parametric uncertainty. Numerical uncertainties are related to the finite time of a dynamic simulation and the intrinsic stochasticity of the kMC method (in turn related to random number generators or the number of independent cases run). Parametric uncertainties stem from errors in parameter values due to noisy or insufficient calculations, or in approximations used to calculate them. In this work we have performed all DFT calculations using best practices as accepted by the electronic structure community. As such, it is difficult to ascertain where the sources of errors may be found without carrying out an exhaustive UQ study. Instead, here we apply a scale factor to two key kinetic parameters and study the effects of the imposed variations on "global" kinetic metrics.

TABLE VI. Nucleation time for ±15% variations of two key parameters in our model. The value calculated for the nominal parameter set is 13.5(±8.5). All values are in seconds.

Parameter	+15%	−15%
E_m^{AB}	16.4(±8.2)	17.7(±8.7)
$E_b^{(a\text{-}d)}$	16.9(±7.5)	24.4(±3.0)

Given the presumably important role of mixed dumbbells in solute transport and cluster nucleation, we have chosen to vary their migration energy by ±15% from its original value of 0.12 eV (E_m^{AB} in Table IV). As well, we have applied the same variation of ±15% to the value of the solute-vacancy binding energy [$E_b^{(a\text{-}d)}$ in Eqs. (17a)–(17d)]. This parameter sets the value of the $\varepsilon_{\text{B-V}}$ bond energy, which depends on the local solute concentration (cf. Table II). The global metrics used to assess the impact of these changes are the nucleation time of 13.5(±8.5) s and the cluster growth rates shown in Fig. 12. Four independent simulations were performed for every parameter change. As shown in Table VI, we find that the changes in E_m^{AB} of ±15% result in nucleation times that are within the natural variability of our kMC simulations. The nucleation times increase by approximately 24%, within the error bars of ≈60% of the standard case. Interestingly, we find no effect whatsoever on the growth rate of the clusters from these changes.

The details of these simulations are provided in the Supplemental Material [77]. For their part, changes of ±15% in $E_b^{(a\text{-}d)}$ seem to have a different effect. The +15% change appears to also have a small measurable impact on the nucleation time, on the same order as changes in E_m^{AB}. However, the negative change results in a value of 24.4(±3.0) s, clearly beyond the statistical error of the nominal nucleation time of 13.5(±8.5) s. This represents a change of +85%, indeed significant. Whether this is a true effect is difficult to establish without a more thorough sensitivity analysis. Also, it is not clear why the effect is nonexistent for the corresponding +15% change.

Where changes in $E_b^{(a\text{-}d)}$ do have a clear impact is on the static phase diagrams in the presence of vacancies, such as those shown in Fig. 7. Indeed, we have seen slight shifts of the phase boundary corresponding to $\eta = 0$ (signaling the transition from phase separation to ordering/solid solution). The rest of the phase diagram remained unaltered. These changes do not modify the overall behavior of the alloy, however, which still displays the same global features as the original results. These phase diagrams are also provided in the Supplemental Material [77].

In any case, changes in the two parameters selected do not appear to change the governing mechanisms of Re cluster formation (as described in Sec. IV A), only the associated time scales. So we preliminarily conclude that variations of up to ±15% in the migration energy of the mixed interstitial have little impact on the nucleation time and cluster growth rates, while a decrease of −15% in the binding energy between vacancies and solute atoms results in an appreciable increase in the nucleation time (although still no effect on the growth rate). The reasons behind this numerical sensitivity are not clear, but

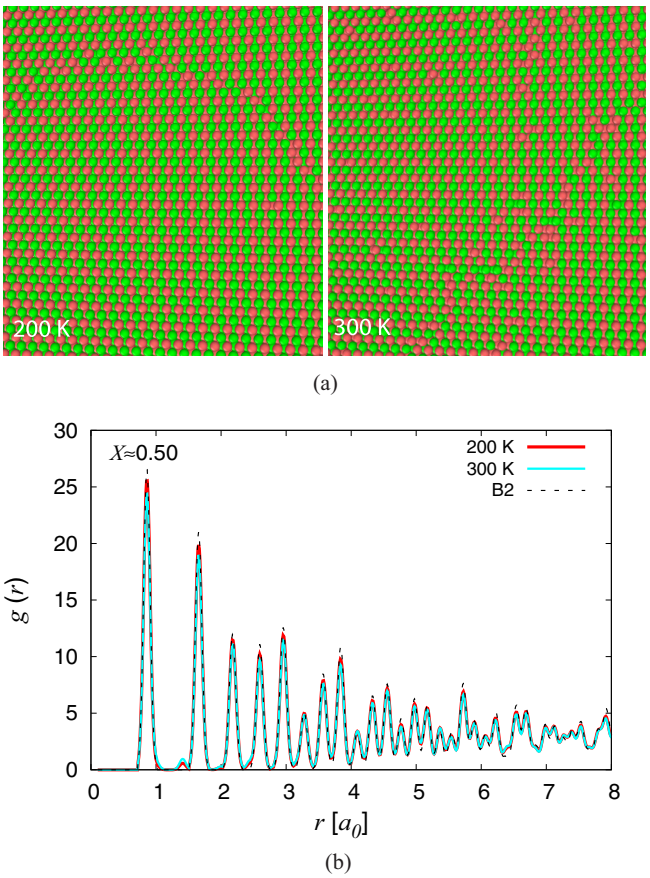

FIG. 16. Atomistic snapshots of the equilibrium configurations of the W-50Re system and associated pair correlation function at 200 and 300 K. (a) $X \approx 0.50$. (b) Pair correlation function.

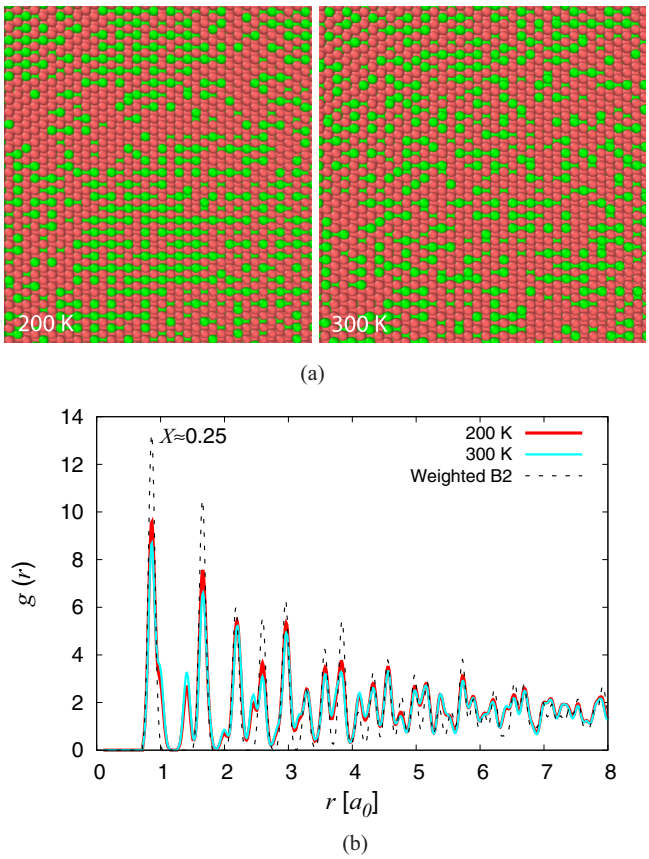

FIG. 17. Atomistic snapshots of the equilibrium configurations of the W-25Re system and associated pair correlation function at 200 and 300 K. (a) $X \approx 0.25$. (b) Pair correlation function.

this limited study gives an idea of the impact of key energetic parameters on the kinetics of cluster nucleation and growth.

ACKNOWLEDGMENTS

The work of C.H., Y.Z., and J.M. has been supported by the US Department of Energy's Office of Fusion Energy Sciences, Grant No. DE-SC0012774:0001. Computer time allocations at UCLA's IDRE Hoffman2 supercomputer are also acknowledged. L.G. and P.E. acknowledge support from the Swedish Research Council and the European Research Council as well as computer time allocations by the Swedish National Infrastructure for Computing at NSC (Linköping) and PDC (Stockholm). Discussions with E. Martinez, X. Hu, and D. Nguyen-Mahn are gratefully acknowledged.

APPENDIX A: ALLOY EQUILIBRIUM STRUCTURES PREDICTED BY SEMI-GRAND-CANONICAL MONTE CARLO SIMULATIONS

The equilibrium structures predicted by our bond energy model are consistent with ordered intermetallics of various types. Here we analyze alloy configurations at concentrations of 25 and 50 at.%, each at 200 and 300 K. Atomistic snapshots for the W-50Re structures are shown in Fig. 16.

The observed atomistic configurations have almost perfect B2 structure. A well-defined phase boundary can be seen in the 200-K image, while more random phase defects are generated at 300 K. Higher temperatures stabilize these defects such that a lot of the order observed in the figure is lost and the system resembles more a random solid solution. The corresponding pair distribution function is shown in Fig. 16(b). An almost perfect match with a reference B2 structure can be clearly appreciated in the figure, confirming the qualitative atomistic picture.

At lower concentrations, the system phase separates into two distinct regions. Effectively, the Re atoms precipitate into clusters of intermetallic B2 phase surrounded by a pure W bcc structure. This phase corresponds to the shaded region in Figs. 6 and 7. The $g(r)$ analysis, shown in Fig. 17(b), is consistent with this picture. We have found no evidence of the formation of other intermetallics based on the bcc lattice such as the $D0_3$ configuration in our simulations.

Therefore, at low temperatures (below approximately 300 K) the energetics of our lattice model predicts a phase-separated system with regions of B2 containing the solute atoms precipitating out in the pure W bcc lattice. As the temperature increases, this weak order is lost in favor of an effective solid solution with small local B2 precipitates internally.

APPENDIX B: SIZE DEPENDENCE OF PHYSICAL TIME IN kMC SIMULATIONS

As explained in Sec. IV, the mechanism of formation of Re clusters requires the concerted action of both interstitials and vacancies. In order to be able to capture their formation during reasonable computational times, the temperature regime considered must be one where the mobility of both species is comparable (1700 ∼ 2000 K in our case). Then, the rate of arrival of solute atoms to a previously-nucleated Re cluster can be approximated by

$$r_s = \frac{1}{t_{\mathrm{FP}} + t_{\mathrm{diff}}}, \tag{B1}$$

where t_{FP} and t_{diff} are the average time in between successive Frenkel-pair insertions and a characteristic diffusion time required by a vacancy and an interstitial to recombine with one another. r_s is measured in units of atoms per unit time. At the temperatures and dose rates considered here, $t_{\mathrm{FP}} \gg t_{\mathrm{diff}}$, such that $r_s \approx {t_{\mathrm{FP}}}^{-1}$. Assuming then that for each Frenkel pair inserted a minimum of one solute atom is transported,

$$r_s = \frac{dN_B}{dt} = r_{\mathrm{dpa}} N, \tag{B2}$$

where N_B is the total number of solute atoms in the precipitate. r_{dpa} in the above equation is the damage rate, expressed in units of dpa s^{-1}. The precipitate volume growth rate is directly equal to the atomic volume times r_s:

$$\dot{V}_{\mathrm{ppt}} = \Omega_a r_s = \Omega_a \frac{dN_B}{dt} = \Omega_a r_{\mathrm{dpa}} N. \tag{B3}$$

Assuming that the precipitate is close to spherical,

$$\dot{V}_{\mathrm{ppt}} = 4\pi R_{\mathrm{ppt}}^2 \dot{R}_{\mathrm{ppt}} = \Omega_a r_{\mathrm{dpa}} N.$$

And, operating, we arrive at the equation for the evolution of the precipitate radius with time:

$$R_{\mathrm{ppt}} = \left(\frac{\Omega_a r_{\mathrm{dpa}} N t}{4\pi} \right)^{\frac{1}{3}}, \tag{B4}$$

which is the equation used for fitting in Fig. 12.

Then, from Eq. (B2), for a given constant dpa rate, it is clear that the ratio $r_s(V_1)N_1^{-1} = r_s(V_2)N_2^{-1} = \text{constant}$, where V_1 and V_2 are two different box sizes. For as long as the approximation in Eq. (B1) is valid, then

$$t_{\mathrm{FP}}^{(1)} N_1 = t_{\mathrm{FP}}^{(2)} N_2 = \text{constant},$$

which allows us to compare simulations done on box sizes of 64^3 and 80^3 directly. We emphasize that at lower temperatures, and/or high dose rate, where $t_{\mathrm{FP}} \approx t_{\mathrm{diff}}$, this comparison is no longer valid.

[1] S. J. Zinkle and N. M. Ghoniem, Fusion Eng. Des. **51-52**, 55 (2000).

[2] M. Rieth, S. L. Dudarev, S. M. Gonzalez de Vicente, J. Aktaa, T. Ahlgren, S. Antusch, D. E. J. Armstrong, M. Balden, N. Baluc, M. F. Barthe, W. W. Basuki, M. Battabyal, C. S. Becquart, D. Blagoeva, H. Boldyryeva, J. Brinkmann, M. Celino, L. Ciupinski, J. B. Correia, A. De Backer, C. Domain, E. Gaganidze, C. García-Rosales, J. Gibson, M. R. Gilbert, S. Giusepponi, B. Gludovatz, H. Greuner, K. Heinola, T. Höschen, A. Hoffmann, N. Holstein, F. Koch, W. Krauss, H. Li, S. Lindig, J. Linke, C. Linsmeier, P. López-Ruiz, H. Maier, J. Matejicek, T. P. Mishra, M. Muhammed, A. Muñoz, M. Muzyk, K. Nordlund, D. Nguyen-Manh, J. Opschoor, N. Ordás, T. Palacios, G. Pintsuk, R. Pippan, J. Reiser, J. Riesch, S. G. Roberts, L. Romaner, M. Rosiński, M. Sanchez, W. Schulmeyer, H. Traxler, A. Ureña, J. G. van der Laan, L. Veleva, S. Wahlberg, M. Walter, T. Weber, T. Weitkamp, S. Wurster, M. A. Yar, J. H. You, and A. Zivelonghi, J. Nucl. Mater. **432**, 482 (2013).

[3] S. P. Fitzgerald and D. Nguyen-Manh, Phys. Rev. Lett. **101**, 115504 (2008).

[4] C. S. Becquart and C. Domain, J. Nucl. Mater. **385**, 223 (2009).

[5] M. R. Gilbert and J.-C. Sublet, Nucl. Fusion **51**, 043005 (2011).

[6] M. R. Gilbert, S. L. Dudarev, S. Zheng, L. W. Packer, and J.-C. Sublet, Nucl. Fusion **52**, 083019 (2012).

[7] J. He, G. Tang, A. Hasegawa, and K. Abe, Nucl. Fusion **46**, 877 (2006).

[8] T. Tanno, A. Hasegawa, J. C. He, M. Fujiwara, M. Satou, S. Nogami, K. Abe, and T. Shishido, J. Nucl. Mater. **386-388**, 218 (2009).

[9] A. Hasegawa, T. Tanno, S. Nogami, and M. Satou, J. Nucl. Mater. **417**, 491 (2011).

[10] X. Hu, T. Koyanagi, M. Fukuda, N. K. Kumar, L. L. Snead, B. D. Wirth, and Y. Katoh, J. Nucl. Mater. **480**, 235 (2016).

[11] X. Hu, T. Koyanagi, Y. Katoh, M. Fukuda, B. D. Wirth, and L. L. Snead, Defect evolution in neutron-irradiated single-crystalline tungsten, in Semiannual Progress Report for Period Ending June 30, 2015, DOE/ER-0313/58.

[12] G. A. Cottrell, J. Nucl. Mater. **334**, 166 (2004).

[13] A. Xu, C. Beck, D. E. Armstrong, K. Rajan, G. D. Smith, P. A. Bagot, and S. G. Roberts, Acta Mater. **87**, 121 (2015).

[14] A. Xu, D. E. Armstrong, C. Beck, M. P. Moody, G. D. Smith, P. A. Bagot, and S. G. Roberts, Acta Mater. **124**, 71 (2017).

[15] M. Ekman, K. Persson, and G. Grimvall, J. Nucl. Mater. **278**, 273 (2000).

[16] S. G. Fries and B. Sundman, Phys. Rev. B **66**, 012203 (2002).

[17] T. Leonhardt, JOM **61**, 68 (2009).

[18] G. S. Was, *Fundamentals of Radiation Materials Science: Metals and Alloys* (Springer Science & Business Media, New York, 2007).

[19] G. J. Dienes and A. Damask, J. Appl. Phys. **29**, 1713 (1958).

[20] R. Cauvin and G. Martin, J. Nucl. Mater. **83**, 67 (1979).

[21] J. S. Wróbel, D. Nguyen-Manh, K. J. Kurzydłowski, and S. L. Dudarev, J. Phys.: Condens. Matter **29**, 145403 (2017).

[22] M. Klimenkov, U. Jäntsch, M. Rieth, H. Schneider, D. Armstrong, J. Gibson, and S. Roberts, Nucl. Mater. Energy **9**, 480 (2016).

[23] J. Matolich, H. Nahm, and J. Moteff, Scr. Metall. **8**, 837 (1974).

[24] V. Sikka and J. Moteff, Metallurgical Mater. Trans. B **5**, 1514 (1974).

[25] R. K. Williams, F. W. Wiffen, J. Bentley, and J. O. Stiegler, Metall. Trans. A **14**, 655 (1983).

[26] R. Herschitz and D. N. Seidman, Acta Metall. **32**, 1155 (1984).

[27] R. Herschitz and D. N. Seidman, Nucl. Instrum. Methods Phys. Res., Sect. B **7**, 137 (1985).

[28] T. Suzudo, M. Yamaguchi, and A. Hasegawa, Modell. Simul. Mater. Sci. Eng. **22**, 075006 (2014).

[29] T. Suzudo, M. Yamaguchi, and A. Hasegawa, J. Nucl. Mater. **467, Part 1**, 418 (2015).

[30] L. Gharaee, J. Marian, and P. Erhart, J. Appl. Phys. **120**, 025901 (2016).

[31] C.-H. Huang and J. Marian, J. Phys.: Condens. Matter **28**, 425201 (2016).

[32] K. Binder, J. L. Lebowitz, M. K. Phani, and M. H. Kalos, Acta Metall. **29**, 1655 (1981).

[33] B. Dunweg and D. P. Landau, Phys. Rev. B **48**, 14182 (1993).

[34] C. Pareige, F. Soisson, G. Martin, and D. Blavette, Acta Mater. **47**, 1889 (1999).

[35] F. Tavazza, D. P. Landau, and J. Adler, Phys. Rev. B **70**, 184103 (2004).

[36] L. Cannavacciuolo and D. P. Landau, Phys. Rev. B **71**, 134104 (2005).

[37] A. Biborski, L. Zosiak, R. Kozubski, R. Sot, and V. Pierron-Bohnes, Intermetallics **18**, 2343 (2010).

[38] The semi-grand-canonical (SG) ensemble employed in the present work is characterized for a two-component system by the following parameters: (i) the total number of sites (or particles) N, (ii) the chemical potential difference between the components μ, (iii) the temperature T, and (iv) the volume V. By contrast, the equivalent grand-canonical (GC) ensemble depends on the number of sites (particles) of type A, N_{A}, and B, N_{B}, as well as T and V. Accordingly, in the GC ensemble the total number of sites (particles) is not constant. While Monte Carlo (MC) simulations of the present kind based on lattice Hamiltonians are occasionally described as GCMC simulations, the fact that the total number of atoms is fixed implies that they should be instead referred to as SGMC simulations.

[39] W. M. Young and E. W. Elcock, Proc. Phys. Soc. **89**, 735 (1966).

[40] F. Soisson, C. S. Becquart, N. Castin, C. Domain, L. Malerba, and E. Vincent, J. Nucl. Mater. **406**, 55 (2010).

[41] F. Soisson, A. Barbu, and G. Martin, Acta Mater. **44**, 3789 (1996).

[42] F. Soisson and C.-C. Fu, Phys. Rev. B **76**, 214102 (2007).

[43] E. Martínez, O. Senninger, C.-C. Fu, and F. Soisson, Phys. Rev. B **86**, 224109 (2012).

[44] O. Senninger, F. Soisson, E. Martínez, M. Nastar, C. Fu, and Y. Brechet, Acta Mater. **103**, 1 (2016).

[45] F. G. Djurabekova, L. Malerba, C. Domain, and C. S. Becquart, Nucl. Instrum. Methods Phys. Res., Sect. B **255**, 47 (2007).

[46] E. Vincent, C. S. Becquart, and C. Domain, J. Nucl. Mater. **382**, 154 (2008).

[47] E. Vincent, C. S. Becquart, C. Pareige, P. Pareige, and C. Domain, J. Nucl. Mater. **373**, 387 (2008).

[48] C. Reina, J. Marian, and M. Ortiz, Phys. Rev. B **84**, 104117 (2011).

[49] W. Zhou, Y. Li, L. Huang, Z. Zeng, and X. Ju, J. Nucl. Mater. **437**, 438 (2013).

[50] L. Gharaee and P. Erhart, J. Nucl. Mater. **467, Part 1**, 448 (2015).

[51] F. Soisson, J. Nucl. Mater. **349**, 235 (2006).

[52] P. Warczok, J. Ženíšek, and E. Kozeschnik, Comput. Mater. Sci. **60**, 59 (2012).

[53] W. Setyawan, G. Nandipati, and R. J. Kurtz, Interaction of interstitial clusters with rhenium, osmium, and tantalum in tungsten, Tech. Rep. DOE/ER-0313/60, 2016.

[54] C. Becquart, C. Domain, U. Sarkar, A. DeBacker, and M. Hou, J. Nucl. Mater. **403**, 75 (2010).

[55] D. Kato, H. Iwakiri, and K. Morishita, J. Nucl. Mater. **417**, 1115 (2011).

[56] W. L. Bragg and E. J. Williams, Proc. R. Soc. London, Ser. A **145**, 699 (1934).

[57] W. L. Bragg and E. J. Williams, Proc. R. Soc. London, Ser. A **151**, 540 (1935).

[58] E. J. Williams, Proc. R. Soc. London, Ser. A **152**, 231 (1935).

[59] C. S. Becquart and C. Domain, Nucl. Instrum. Methods Phys. Res., Sect. B **255**, 23 (2007).

[60] L. Ventelon, F. Willaime, C.-C. Fu, M. Heran, and I. Ginoux, J. Nucl. Mater. **425**, 16 (2012).

[61] M. Muzyk, D. Nguyen-Manh, K. J. Kurzydłowski, N. L. Baluc, and S. L. Dudarev, Phys. Rev. B **84**, 104115 (2011).

[62] Y. Oda, A. M. Ito, A. Takayama, and H. Nakamura, Plasma Fusion Res. **9**, 3401117 (2014).

[63] M. R. Gilbert, S. L. Dudarev, P. M. Derlet, and D. G. Pettifor, J. Phys.: Condens. Matter **20**, 345214 (2008).

[64] P. E. Blöchl, Phys. Rev. B **50**, 17953 (1994).

[65] G. Kresse and D. Joubert, Phys. Rev. B **59**, 1758 (1999).

[66] G. Kresse and J. Hafner, Phys. Rev. B **47**, 558 (1993).

[67] G. Kresse and J. Hafner, Phys. Rev. B **49**, 14251 (1994).

[68] G. Kresse and J. Furthmüller, Phys. Rev. B **54**, 11169 (1996).

[69] G. Kresse and J. Furthmüller, Comput. Mater. Sci. **6**, 15 (1996).

[70] J. P. Perdew, K. Burke, and M. Ernzerhof, Phys. Rev. Lett. **77**, 3865 (1996); **78**, 1396(E) (1997).

[71] G. Henkelman, B. P. Uberuaga, and H. Jónsson, J. Chem. Phys. **113**, 9901 (2000).

[72] J. M. Cowley, Phys. Rev. **77**, 669 (1950).

[73] T. Tanno, A. Hasegawa, J.-C. He, M. Fujiwara, S. Nogami, M. Satou, T. Shishido, and K. Abe, Mater. Trans. **48**, 2399 (2007).

[74] Y. Le Bouar and F. Soisson, Phys. Rev. B **65**, 094103 (2002).

[75] M. Nastar and F. Soisson, Phys. Rev. B **86**, 220102 (2012).

[76] A. Allnatt and A. Lidiard, *Atomic Transport in Solids* (Cambridge University Press, Cambridge, 2003).

[77] See Supplemental Material at http://link.aps.org/supplemental/10.1103/PhysRevB.96.094108 for additional details about the simulations referred to in the main text.

[78] P. D. Edmondson, A. Xu, L. R. Hanna, M. Dagan, S. G. Roberts, and L. L. Snead, Microsc. Microanal. **21**, 579 (2015).

[79] T. Tanno, A. Hasegawa, M. Fujiwara, J.-C. He, S. Nogami, M. Satou, T. Shishido, and K. Abe, Mater. Trans. **49**, 2259 (2008).

[80] P. Erhart, J. Marian, and B. Sadigh, Phys. Rev. B **88**, 024116 (2013).

[81] A. E. Sand, S. L. Dudarev, and K. Nordlund, Europhys. Lett. **103**, 46003 (2013).

[82] X. Yi, A. E. Sand, D. R. Mason, M. A. Kirk, S. G. Roberts, K. Nordlund, and S. L. Dudarev, Europhys. Lett. **110**, 36001 (2015).

[83] W. Setyawan, G. Nandipati, K. J. Roche, H. L. Heinisch, B. D. Wirth, and R. J. Kurtz, J. Nucl. Mater. **462**, 329 (2015).

[84] D. Terentyev, L. Malerba, and A. V. Barashev, Philos. Mag. Lett. **85**, 587 (2005).